

POLITECNICO DI TORINO

DEPARTMENT OF MECHANICAL AND AEROSPACE ENGINEERING

Master's Degree Course in Biomedical Engineering



Academic Year 2020/2021

***In silico* biomechanical evaluation of an innovative
intramedullary interphalangeal nail in Nitinol**

Candidate

Marco Bonfanti

Supervisors

Ing. Dario Carbonaro

Ing. Mara Terzini

Prof. Alberto Audenino

December 2021

Contents

Contents.....	I
Abbreviations.....	III
Abstract.....	V
Introduction	VII
1. Interphalangeal joint: anatomy and pathology	- 1 -
1.1. Arthritis	- 2 -
1.2. Lesser toe deformities	- 3 -
2. Interphalangeal joint arthrodesis.....	- 5 -
2.1. Gold standard in small bone fixation	- 5 -
2.2. Intramedullary interphalangeal Nitinol implants	- 6 -
2.2.1. Nitinol.....	- 7 -
2.2.1.1. Shape memory and superelasticity.....	- 8 -
2.2.1.2. Fatigue behavior.....	- 12 -
2.2.1.3. Biocompatibility	- 12 -
2.2.1.4. Material behavior in finite element analyses	- 14 -
2.2.2. Devices on the market	- 15 -
2.2.3. Device design	- 17 -
2.2.4. Regulation.....	- 21 -
2.2.5. State of the art finite element analysis.....	- 23 -
3. Materials and Methods	- 27 -
3.1. Geometrical model	- 28 -
3.2. Finite element model	- 29 -
3.3. Finite element analysis	- 31 -
3.3.1. Model verification	- 31 -
3.3.2. Bending of the implant	- 32 -
3.3.3. Fatigue assessment	- 33 -
3.3.4. Expansion and anchoring of the implant	- 37 -
4. Result.....	- 41 -
4.1. Model verification	- 41 -
4.2. Bending of the implant.....	- 42 -
4.3. Fatigue assessment	- 45 -
4.4. Expansion and anchoring of the implant.....	- 45 -
5. Discussion.....	- 51 -
5.1. Model verification	- 51 -
5.2. Bending of the implant.....	- 52 -

5.3.	Fatigue assessment	- 54 -
5.4.	Expansion and anchoring of the implant	- 55 -
5.5.	Limits.....	- 56 -
6.	Conclusion	- 59 -
	References	- 61 -

Abbreviations

ASTM	American Society for Testing and Materials International
DIP	Distal Interphalangeal
COF	Coefficient of friction
FDA	Food and Drug Administration
FE	Finite Element
IINI	Intramedullary Interphalangeal Nitinol Implants
IMFD	Intramedullary Fixation Device
K-wires	Kirschner wires
MCP	Metacarpophalangeal
MTP	Metatarsophalangeal
PIP	Proximal Interphalangeal
SMA	Shape Memory Alloy

Abstract

Arthrodesis is a reliable alternative to conservative treatments in handling intractable arthritic pain and joint deformity. Temporary Kirschner wires are a widely adopted solution to perform arthrodesis, however, they do not provide compression in the joint and do not control the phalanx rotation, with an associated risk of infection, breakage, migration, and discomfort for the patient. To overcome these limitations, permanent intramedullary interphalangeal Nitinol implants (IINIs) have been recently developed. These innovative devices exploit the shape memory effect and superelasticity of Nitinol to change their shape once implanted in the body in order to anchor to the bone and provide compression at the arthrodesis site. Within this context, Finite Element (FE) method is an efficient tool to assist the devices design process and achieve better clinical outcomes. *In silico* simulations are playing an increasingly decisive role in evaluating the mechanical performance of medical devices and providing evidence for their certification.

In this perspective, this work aims to define a numerical framework to evaluate the biomechanical behavior of an IINI. Two FE simulations were conducted on a three-dimensional model of the IINI Stryker Smart Toe II. The geometry was created by reproducing drawings and measurements publicly available, was meshed with tetrahedral elements and a superelastic behavior of Nitinol was used. The first test aims to reproduce *in silico* the push-off phase of gait in order to identify the most stressed areas and provide an estimate of the bending force and displacement the nail can support. Therefore, the proximal part of the device was constrained while the distal part was flexed upward. The second test allows to determine the contact forces between bone and implant once it has expanded into the medullary canal. The nail was initially compressed into its pre-implant form and then gradually expanded. The anchor force was consequently computed, predicting the risk of bone non-union and implant migration.

The simulations conducted enabled to identify critical areas for structural failure, to predict the maximum supportable loads and to compute the anchorage forces. To conclude, the proposed FE analyzes could minimize the device development costs and times while improving the quality of the product and providing useful information for achieving certification.

Introduction

The thesis is part of "Nitoliera" project, a research supported by Regione Piemonte, born from the collaboration between Politecnico di Torino, LAMP srl, AortiLab srl, and Intrauma spa, for the creation of a new Nitinol supply chain. LAMP is a manufacturing company that will bring the first Nitinol production line in Italy, while AorticLab and Intrauma will produce endovascular and orthopedic medical devices, respectively, using Nitinol as raw material. Politecnico di Torino will assist the entire process.

In particular, this work was accomplished with the Turin-based company Intrauma. The goal of the collaboration is the creation of an intramedullary interphalangeal Nitinol implants (IINI) for small bone fixation, reconstruction and fusion. Nitinol is a material with peculiar properties and, in this work, the framework developed using FE modeling provided a state-of-the-art method to evaluate the biomechanical performance of an example device providing useful information for its certification.

The thesis work is organized as follows:

Chapter 1 introduces the anatomy of the hands and feet by focusing on the phalanges and joints. Arthritis and lesser toe deformities, two of the main pathologies that can be treated with arthrodesis, are then described.

Chapter 2 begins introducing arthrodesis. Subsequently the standard technique to perform it and the innovative alternative of IINIs are illustrated. IINI are analyzed from different point of view: from the material they are made of to the design and the state of the art of FE analysis on these new devices.

Chapter 3 describes the methods used to reproduce the three-dimensional model of the Nitinol implant Smart Toe II and the methods applied to create its FE model. Finally are described the two *in silico* simulations implemented in this work and the rationale behind their choice.

Chapter 4 shows the results obtained from the simulations. For the sake of simplicity, the results of the first simulation, analysis of the stress-strains and bending moments, are divided from the results of the second simulation where, in addition to stress-strains, the contact and anchor forces are studied. In *Chapter 5* the results obtained in the previous chapter are discussed maintaining the distinction between the first and second simulation. In addition, insights on further information derived from the results obtained and the list of limitations of this work are presented.

Chapter 6 concludes the thesis with some considerations on the work done, the impact on the device design process and possible future developments.

1. Interphalangeal joint: anatomy and pathology

The hand is the distal end of each upper limb of the human body. Equipped with 5 fingers, it has a structure that includes bones, joints, ligaments, muscles and tendons. It allows to grasp objects, acts as a tactile sense organ and permits communication. The foot is at the distal end of each lower limb of the human body. Culminating with 5 fingers, it has a structure similar to the hand. It is the fixed point on the ground on which the entire weight of the body rests. It is the basis of the balance system and allows to assume an upright posture and move in space. Like the hand, the foot is both an effector and a receptor, it receives and executes commands through the muscles, and at the same time, it interacts with the rest of the body providing constant information coming from its proprioceptors. The foot is mainly divided into three parts: heel, metatarsal bones and toes, for a total of 26 bones. The forefoot is the anterior portion of the foot that includes the metatarsal bones and the phalanges of the toes. Similarly, the hand can be divided into three parts: carpus, metacarpus and fingers. Both hand and foot can be divided into five lesser rays. Each lesser foot (hand) ray is composed of a metatarsal (metacarpal) bone and the phalanges, which are classified in proximal, middle, and distal according to the distance from the center of the body. These four components are interconnected via three joints. The interphalangeal joints are uniaxial (hinge) synovial joints that usually allow flexion without extension. They can be divided into: distal interphalangeal (DIP) joints, between the middle and distal phalanges, and proximal interphalangeal (PIP) joints, between the proximal and middle phalanges. Metacarpophalangeal (MCP) and metatarsophalangeal (MTP) joints are condyloid joints and allow the movements of flexion, extension, abduction, adduction and circumduction at the joint. They are between the metacarpal or metatarsal bones and proximal phalanges [1].

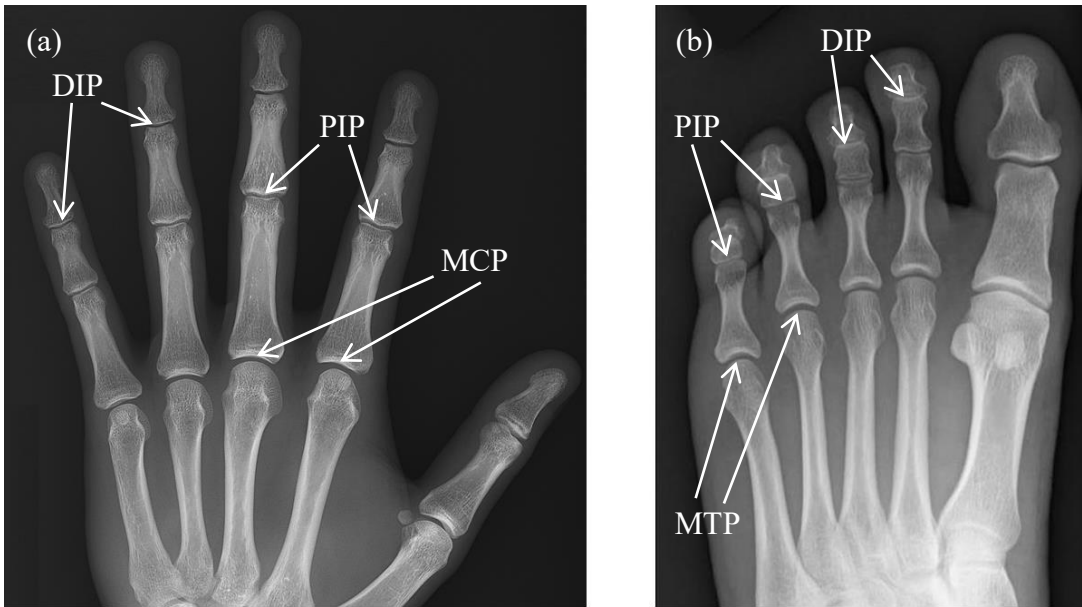


Figure 1-1: Hands (a) and foot (b) joints. DIP = distal interphalangeal; PIP = proximal interphalangeal; MCP = metacarpophalangeal; MTP = metatarsophalangeal. Picture adapted from [2], [3].

Instability associated with arthrosis or traumatic conditions and finger or toe deformities are the main pathologies affecting joints whose treatment includes interphalangeal joint arthrodesis.

1.1. Arthritis

Arthritis is an umbrella term to refer to joint pain or joint disease. The type of arthritis depends on the origin of the causes, which can be traumatic, metabolic, infectious, autoimmune, or idiopathic. The most common type of arthritis is osteoarthritis, followed by rheumatoid arthritis. Osteoarthritis is characterized by an inflammatory state that causes a progressive deterioration of the cartilage layer that covers the joint surfaces. It mainly affects the joints of the hand, knees and spine. Rheumatoid arthritis is an autoimmune disease that attacks the synovial membrane of the joints, damaging the joint surfaces and cartilage. In the beginning, the inflammation mainly affects the joints of the toes and fingers.

When fingers are affected by degenerative, inflammatory, posttraumatic arthritis and/or joint instability, the subject often feels pain and the function of the hand is reduced. In this case, arthrodesis is a reliable surgical choice in the treatment of intractable arthritic pain, joint deformity, and instability when conservative treatments failed [4], [5]. It is also indicated for chronic mallet finger deformity and avulsion of the flexor digitorum profundus [5]. An alternative to arthrodesis is arthroplasty, however, the latter is mainly performed to correct PIP joint deformities, while arthrodesis is preferred in DIP, thumb inter-phalangeal joint, and MTP joint [4].

1.2. Lesser toe deformities

Lesser toe deformities are one of the most frequent pathologies of the forefoot and include mallet toe, hammer toe, claw toe, curly toe, and crossover toe. The incidence of claw toe or hammertoe varies between 20 and 30% [6]–[8].

In mallet toe the DIP joint has a flexion deformity with the PIP and MTP joints in a neutral position. It can be caused by rupture or laceration of the extensor digitorum longus at the DIP joint or pressure of the toe against the end of the shoe (DIP flexion and tightness of the flexor digitorum longus) [1].

A hammer toe is defined as either a rigid or flexible deformity of the lesser toes involving flexion of the PIP joint [9]. It is commonly accepted that hammer toe is characterized by a MTP extension combined with a PIP flexion position and claw toe by a MTP extension with flexion of the PIP and DIP joints [10]. The discrimination between hammer toe and claw toe can also be performed based on the state of the MTP joint[10]. In fact, claw toe can be defined as a hammer toe deformity with extension into the MTP joint, as a continuum of the pathophysiologic process [11]. A fixed flexion deformity at the PIP joint can be therefore defined as hammer toe as long as the MTP joint is flexible and claw toe can be defined as an extension contracture in the MTP joint with a decline in function. However, the exact definition of hammer toe and the distinction with claw toe is still a source of debate.

Curly toe deformity is similar to claw toe but MTP is either neutral or in flexion and typically has a rotational component. It is most commonly seen in the fifth toe in children and is caused by contracture of the flexor digitorum longus and flexor digitorum brevis.

In Table 1-1 are summarized the joint position associated with each lesser toe deformity.

Table 1-1: Lesser toe deformity features. Adapted from [1].

Deformity	Joint		
	MTP	PIP	DIP
Mallet toe	Neutral	Neutral	Flexed
Hammer toe	Extended or neutral	Flexed	Extended, neutral or flexed
Claw toe	Extended	Flexed	Flexed
Curly toe	Neutral or flexed	Flexed	Flexed
Crossover toe	Unstable (medial or lateral deviation)	Neutral or flexed	Extended, neutral or flexed

DIP = distal interphalangeal; MTP = metatarsophalangeal; PIP = proximal interphalangeal

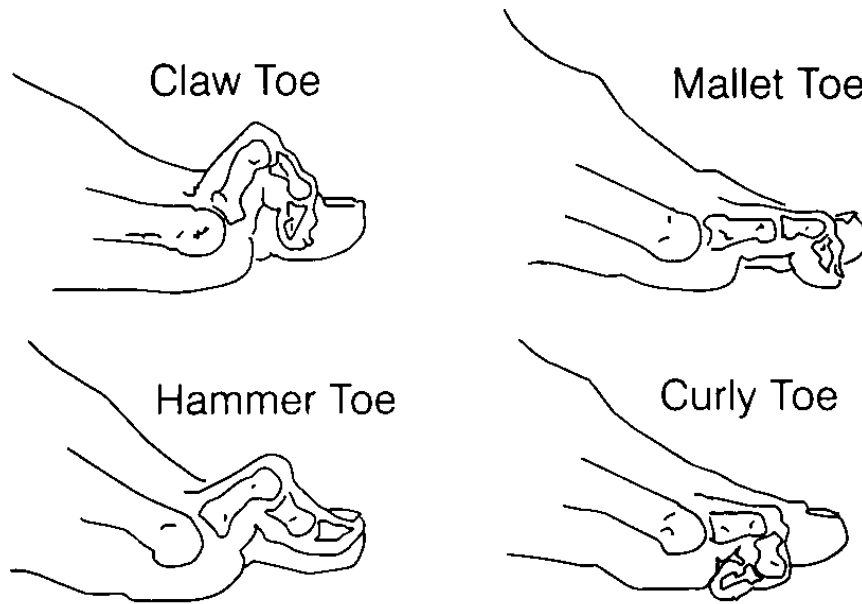


Figure 1-2: : Lateral foot view showing different toe deformity. Picture adapted from [12].

Lesser digital deformities are among the most common problems encountered by the foot and ankle surgeons. Generally, the surgical procedures to correct these deformities can be divided into soft tissue procedures, which include tendon lengthening or flexor digitorum longus tendon transfers [13], and osseous procedures which include joint arthroplasty or arthrodesis [14]. In the case of a spastic or fixed deformity of the digit, the technique that provides the most predictable outcome is arthrodesis which is also the most often chosen surgical procedure [15].

2. Interphalangeal joint arthrodesis

When non-surgical solutions fail in correcting the toe deformity or in reducing the pain associated to the arthritis, the treatment can be addressed with joint resection arthroplasty or fusion, in order to rigidly fix the joint in a well-aligned position [9]. Arthrodesis is the surgical procedure aimed to induce a joint ossification between two bones, it can also be defined as artificial ankylosis. This repair can be achieved by both bony fusion or fibrous union that leads to ankylosis of the joint [16]. As previously mentioned it is often performed to relieve intractable pain in the hands, feet, and spine. It is also performed in the ankle, knee, and hip but with the improvement of biomedical technologies, arthroplasty is now preferred in these cases [17]. Arthrodesis can be addressed by means of bone grafts which may come from autologous bone transplants, usually preferred, allogeneic bone transplants, or synthetic bone. Alternatively, metal fixation devices such as nails, screws, plates, cages, and Kirschner wires (K-wires) can also be used.

2.1. Gold standard in small bone fixation

Although there is no official guideline available to guide the doctors in the choice of the optimal device for interphalangeal joint arthrodesis, for PIP joint deformity correction the use of K-wires has been the widely adopted solution for more than 10 decades [6].



Figure 2-1 : (a) Preoperative radiograph showing hammertoe deformity. (b) Postoperative radiograph of hammertoe correction performed with Kirschner wires. Figure adapted from [18].

Temporary K-wires fixation for 3 to 6 weeks have been proven to be highly successful and with few complications [9]. In the retrospective reviewed conducted by Kramer et al. [18] on 2'698 hammer-toe corrections the reported complication rate were: pin migration (3.5%), pin tract infection (0.3%), pin breakage (0.1%), recurrent deformities (5.6%), revision surgery (3.5%), malalignment (2.1%), vascular compromise (0.6%) and amputation of toe (0.4%). However, the percentages reported are indicative and vary according to the study in question. For example, Zingas et al. [19] review a total of 1002 K-wires placed across the MTP joints and reported a higher rate of rupture of 3.3%, more than thirty times greater.

Although this technique is widely used in clinical practice, it has some criticalities: K-wires do not provide compression in the joint, do not control the phalanx rotation, bony fusion is not always obtained after pin removal, leading to malposition [20]. Moreover, remains a concern regarding exposed temporary K-wire fixation [21], which raises a risk of infection, breakage, migration, and discomfort for the patient [22]–[24]. To overcome these problems, several permanent internal fixation devices, that do not require reoperation, have been recently developed. These can be divided into four categories according to technical features and material composition [25]:

- i. Shape memory or superelastic devices: composed in Nitinol, change their shape once implanted by increasing the anchoring force and bringing the phalanges closer.
- ii. Bone allograft dowels: characterized by bone inductive and conductive properties, which significantly improve their integration.
- iii. One-piece solid or cannulated devices: while the distal part is anchored to the middle phalange, the proximal part is threaded and screwed onto the proximal phalange. Usually are made of steel, titanium or polyetheretherketone.
- iv. Two-piece devices: composed of a female and a male part, one is inserted into the proximal phalanges and the other into the distal phalanges. One positioned, these components are fixed together. Usually are made of titanium or polyetheretherketone.
- v. Absorbable intramedullary implants.

This work will focus on shape memory and superelastic Nitinol devices, the intramedullary interphalangeal Nitinol implants.

2.2. Intramedullary interphalangeal Nitinol implants

IINIs are indicated for small bone fixation, reconstruction and fusion, limited to the inter-digital fusion of fingers and toes. [26]–[29]

They are nails composed of two ends, one is inserted in the distal phalanx and the other in the proximal phalanx. The ends anchor to the medullary canals and keep the two bony extremities in

contact. The peculiar feature that distinguishes them from other nails is the ability to change their shape when subjected to specific temperature variations. This characteristic is conferred by the shape memory effect and superelasticity of Nitinol.

2.2.1. Nitinol

Nitinol is a metal alloy composed of nickel and titanium in almost equal parts. The story that leads to its discovery is one of the abundant examples of serendipity that characterize some inventions in science and technology.

William J. Buehler was a metallurgist at the Naval Ordnance Laboratory. Hired in 1948, he worked on a materials project which had the goal of developing metallic materials for the nose cone of the U.S. Navy Polaris reentry vehicle (part of a Submarine-launched ballistic missile) [30]. In 1959 Buehler decided to concentrate on an equiatomic composition alloy, studied from the *Constitution of Binary Alloys book* [31], and he named his discovery NITINOL (Nickel Titanium Naval Ordnance Laboratory).

One day Buehler dropped a cooled Nitinol bar extracted from an arc-melting furnace on the laboratory floor and observed that the impact produced a dull sound, as if the bar was made of lead. Triggering the concern that the arc-casting process could produce a multitude of micro cracks inside the bar, thus producing unexpected damping phenomena, he decided to drop the other (warmer) bars as well. To his amazement, he observed that these, instead, produced a sound similar to a bell [30]. The discovery of the acoustic damping variation during small temperature changes was followed by another episode of serendipity which led to the observation of the shape memory effect for the first time. During a laboratory management meeting, a 0.25 mm thick long strip of Nitinol was brought to demonstrate the material's unique fatigue-resistant properties. The strip was bent into short folds longitudinally, forming a sort of accordion that was compressed and stretched repeatedly and rapidly without breaking. While the object was passing between the participants, one of them, Dr. David S. Muzzey, applied heat from his pipe lighter to the compressed strip and to everyone's amazement, the sheet of nitinol stretched out longitudinally and regained its original flat shape [32]. The shape memory property of Nitinol was discovered.

In 1962 Dr. Frederick E. Wang, crystal physics expert, joined Buehler's group at the Naval Ordnance Laboratory [33]. He discovered how the shape memory property of Nitinol works and made possible the spread of Nitinol commercial applications over the next few years.

The first successful Nitinol product was the Raychem Corporation's Cryofit™ "shrink-to-fit" pipe coupler, introduced in 1969 to solve the problem of coupling hydraulic-fluid lines in the F-14 jet fighter built by the Grumman Aerospace Corporation [33]. The first biomedical application dates back to 1976, used in orthodontic archwires [34]. In September 1989 the U.S. Food and Drug

Administration (FDA) approved the first Nitinol based implant, the Mitek Surgical Products' Mitek Anchor [Figure 2-2 (a)]. Previously torn ligaments and tendons were treated by immobilizing the limb of the patient in the hope that tissue will grow back or surgery with screws or staples. Mitek's anchor, shaped like a tiny anchor with two arms that hook into the bones, can be implanted through a small incision in its compressed conformation, and after being inserted into the body (at 37°C), thanks to the property of Nitinol, it returns to its original anchor shape. In the same year the radiologist Morris Simon, M.D. of Boston's Beth Israel Medical Center patented a design for a blood filter that can be set in a vein to trap blood clots without surgery [Figure 2-2 (b)] [35]. The device is placed into a large vein through a catheter in straight conformation maintained by a cold saline solution. When warmed to body temperature, the Nitinol wires spring back into their original mushroom shape and attach to the wall of the vein.



Figure 2-2: (a) Mitek Anchor; (b) Simon's filter original mushroom shape. Picture adapted from [36], [37].

2.2.1.1. Shape memory and superelasticity

In this section the terminologies and abbreviations used to describe the characteristic temperatures, phase and behavior of Nitinol comply with the ASTM F2005 standard [38].

Table 2-1: Standard Terminology for Nickel-Titanium Shape Memory Alloys from ASTM F2005-21

Symbol	Definition	Description
A_f	austenite finish temperature	the temperature at which the martensite to austenite transformation is completed on heating in a single-stage transformation.
	austenite	the high temperature parent phase in Ni-Ti shape memory alloys with a B2 crystal structure.
A_s	austenite start temperature	the temperature at which the martensite to austenite transformation begins on heating in a single-stage transformation.
	martensite	the lowest temperature phase in Ni-Ti shape memory alloys with a B19' monoclinic crystal structure.

M_d	martensite deformation temperature	the highest temperature at which martensite will form from the austenite phase in response to an applied stress.
M_f	martensite finish temperature	the temperature at which the transformation from austenite to martensite is completed on cooling in a single-stage transformation.
M_s	martensite start temperature	the temperature at which the transformation from austenite to martensite begins on cooling in a single-stage transformation.
	shape memory alloy	a metal which, after an apparent plastic deformation in the martensitic phase, undergoes a thermoelastic change in crystal structure when heated through its transformation temperature range, resulting in a recovery of the deformation
	superelasticity	nonlinear recoverable deformation behavior of Ni-Ti shape memory alloys at temperatures above the austenite finish temperature (A_f).

Nitinol alloys are composed of two phases: austenitic phase, stable at high temperatures and martensitic phase, stable at lower temperatures. Austenite has similar properties to titanium and is stronger and harder than martensite which is soft and malleable. In fact, Martensite has a self-accommodating twins structure that can be easily deformed by de-twinning the structure when applying stress [39]. The property that distinguishes Nitinol from other alloys is its capability to undergo phase transformation triggered by either thermal or mechanical stimuli. The crystallographic transformation from martensite to austenite and vice versa is reversible. The direct transformation (austenite \rightarrow martensite) occurs when stress is applied or the temperature is reduced; it starts when cooled to M_s and completes at M_f ($M_s > M_f$). The reverse transformation (martensite \rightarrow austenite) occurs when the external load is removed or the temperature is increased; it begins when heated to A_s and is completed at A_f ($A_s < A_f$). Since $A_s > M_f$ and $M_s < A_f$, when the percentage of austenite is plotted as a function of temperature (Figure 2-3), a thermal hysteresis cycle is observed involving the direct and reverse transformations.

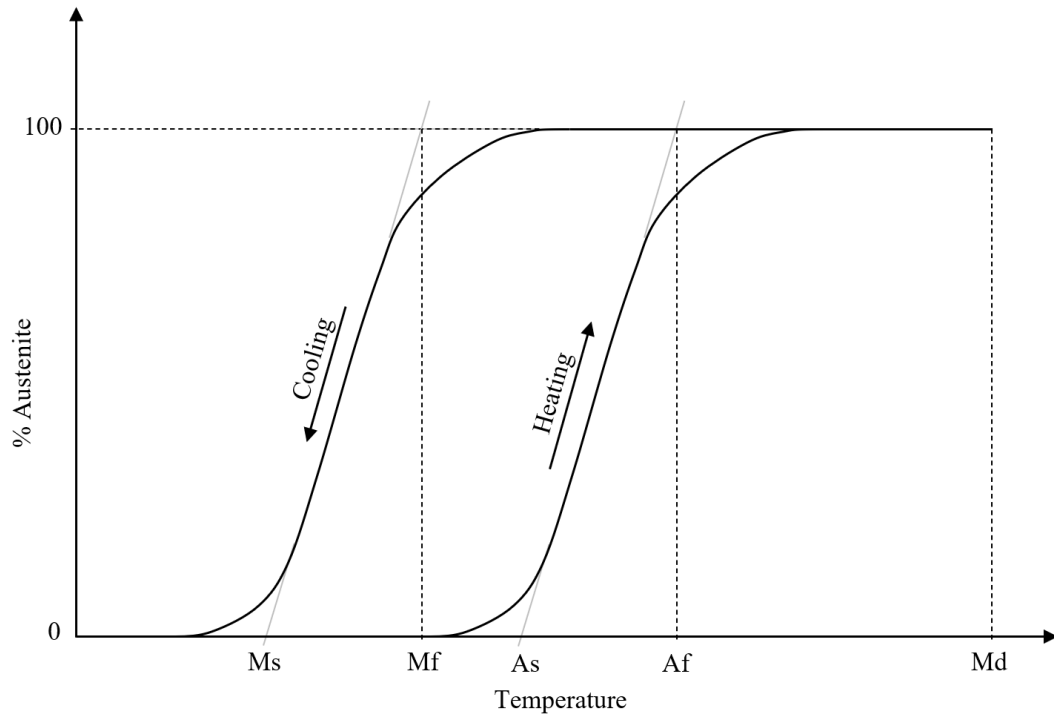


Figure 2-3: Percentage of austenite as a function of temperature. Direct and reverse transformations from austenite to martensite show a hysteresis cycle. Af = austenite finish temperature ; As = austenite start temperature; Md = martensite deformation temperature; Mf = martensite finish temperature; Ms = martensite start temperature.

In the direct transformation, atoms produce a rearrangement within the material, forming a new, more stable crystalline phase with the same chemical composition because the maximum displacement of each atom is less than the interatomic distance and therefore there is no breaking of the chemical bonds.

The transformation of the austenitic phase into the martensitic phase is the result of two simultaneous processes: Bain strain and lattice-invariant shear. Bain strain consists of a series of atomic movements on a small scale (less than interatomic distances) without diffusion phenomena. However, the martensite obtained from this transformation has a macroscopic shape different from the original of the austenitic phase. Therefore, it is necessary that the surrounding austenite and the new martensitic phase find an accommodation of the new structure within the material. Lattice-invariant shear allows this accommodation by means of the twinning mechanism, a reversible process of motion of the atoms facing a plane called twin boundary, which allows the material to take the same original macroscopic shape while preserving the newly formed martensitic structure [40].

Shape memory is a term used to define a metal alloy that in the martensitic phase can be plastically deformed and, when heated to the austenitic phase, spontaneously returns to its previous undeformed shape [39].

At high temperatures ($T > M_d$) the object, characterized by an austenitic structure, is plastically deformed into the original shape (“remembered” shape) that it will assume during usage at $T > A_f$ [Figure 2-4 (a)]. After cooling ($T < M_f$), the austenitic phase transforms to twinned martensite phase and the macroscopic shape remains unchanged [Figure 2-4 (b)]. When, at $T < A_f$, stress is applied above the elastic limit [Figure 2-4 (c)] the object undergoes an apparently plastic deformation into a particular desired shape [Figure 2-4 (d)]. In this process the detwinning takes place: it consists of a reorientation of the planes without breaking the bonds between the atoms which leads to a reversible deformation of the object shape. In fact, when the object is heated at $T > A_f$, as the martensite transforms to austenite the metal gradually recovers its original shape [Figure 2-4 (a)]. If the object is cooled, the shape does not change.

Superelasticity (or pseudoelasticity) is the property that allows Nitinol to exhibit an ultra-high elastic behavior when stressed at temperatures between A_f and M_d (Figure 2-3 and Figure 2-4). Unlike other metals, Nitinol deformation up to 10% strain can be elastically recovered; conversely, for example, steel has 0.5% reversible strain [39]. When stress is applied, the material deforms and the alloy changes from the austenitic phase to the martensitic phase [Figure 2-4 (e)]. More precisely, is obtained a stress-induced martensite which, being at $T > A_f$, is unstable and as soon as the stress is removed, the alloy reverts to the austenite phase and the object to its original shape [Figure 2-4 (a)].

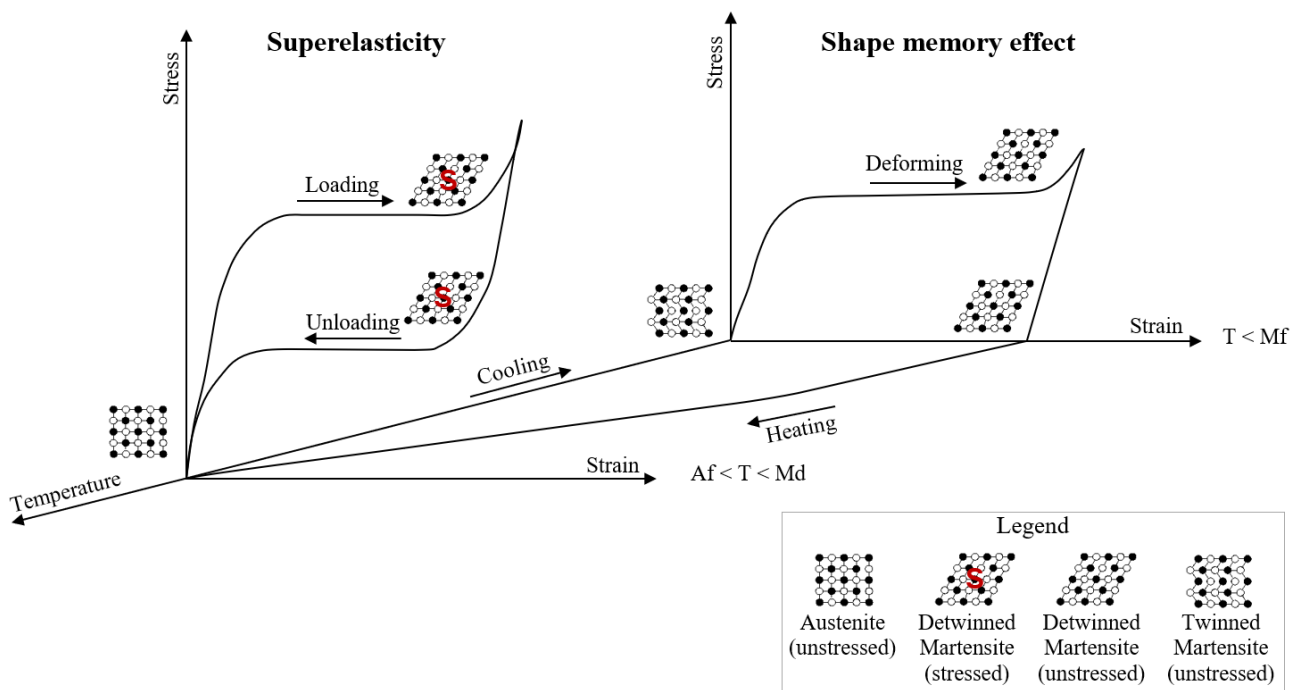


Figure 2-4: Behavior of superelasticity and shape memory effect according to the phase transformation, temperature, stress and strain. A_f = austenite finish temperature ; M_d = martensite deformation temperature; M_f = martensite finish temperature.

2.2.1.2. Fatigue behavior

Fatigue can be either strain controlled or stress controlled. Unlike traditional materials, Nitinol can fatigue more rapidly in stress-controlled situations of cyclic loading because of its strain-dependent fatigue life [41].

In the FDA Guidance for Industry and Food and Drug Administration Staff “Technical Considerations for Non-Clinical Assessment of Medical Devices Containing Nitinol” [42] is stated that stress-based fatigue life estimator (e.g., Goodman, Soderberg diagrams) are not suitable for Nitinol devices. While a constant life mean versus alternating strain diagram has been found to provide a good model for fatigue life prediction for nitinol [43]. The FDA Guidance recommends to carry out the tests on samples that represent the final manufactured device also considering any heat treatments, surface processing and pre-strain, since these factors positively or negatively affect the fatigue life.

Moreover, the concept of structural fatigue in Nitinol devices can be expanded to include also the durability of the shape memory effect and its thermomechanical properties. Hoh et al. [41] identified three modes of fatigue which can be summarized as:

- i. classical fatigue which is the result of cyclic deformations that lead to the formation of defects in the microstructure up to the generation of cracks;
- ii. fatigue of shape memory effect which leads to the loss of recovery of the original shape afterward thermal or mechanical cycles;
- iii. thermomechanical fatigue which manifests itself as an alteration of the hysteresis cycle and transformation temperature when subjected to repeated cycles of crystallographic transformations.

2.2.1.3. Biocompatibility

Before discussing the biocompatibility of a biomaterial it is necessary to define what is meant by biomaterial. The definition is constantly evolving, to date we can rely on the definition proposed in the II International Consensus Conference on Biomaterials hold in Chester, Great Britain, in 1991: “A biomaterial is a material intended to interface with biological systems to evaluate, treat, augment or replace any tissue, organ or function of the body” [44].

Many definitions of biocompatibility exist, the most widely used is William's definition which in the *European Society for Biomaterials Consensus Conference I* defined biocompatibility as "The ability of a material to perform with an appropriate host response in a specific application" [45]. However, according to William himself we should move towards a more specific definitions within

each of the varied applications of biomaterials moving the definition of biocompatibility from a materials base to an applications base definition [46].

The development of biomaterials for medical applications has evolved through three generations [47]:

- First generation (1950s): materials with functional properties suitable for replacement of damaged tissue, and capable of not provoking negative responses from the host organism. These materials are not developed specifically for biomedical applications, but are borrowed from other industries as they possess properties that make them suitable for clinical applications. These materials are defined as *bioinert* because they do not trigger any reaction in the host organism and therefore they are considered biocompatible.
- Second generation (1975): defined as *bioactive* because they elicit controlled and desired responses in the tissue in which they are implanted. In the same years the concept of resorbable biomaterials with degradation rates compatible with the demands deriving from the type of application was also developed; in this way, the material is degraded by the body and replaced with newly formed tissue
- Third generation (2000): stimulate precise reactions at the molecular level. These materials lend themselves to the development of scaffolds capable of attracting endogenous cells in vivo or being seeded with cells in vitro and then implanted. With the advances in tissue engineering and regenerative medicine, a scaffold with specific structural chemical information can control tissue formation by mimicking cell-to-cell communications. Materials belonging to this category are defined as *biomimetic*.

Therefore biomaterials can be categorized according to the response they elicit from living tissues in: biotoxic, bioinert, bioactive, bio-absorbable or biomimetic. But generally, they can be also categorized according to their chemical nature into: polymeric, metallic, ceramic, glass, glass-ceramic, or from biological derivation. Nitinol is a metallic bioinert material.

The biocompatibility of Nitinol has different characteristics deriving from the biocompatibility of the single elements that make up the alloy. Titanium or nickel ions could dissolve during the corrosion process, therefore it is important to investigate the effects that these elements produce.

It is currently accepted that pure titanium is very well tolerated by local tissues [48]. Thanks to the formation of a superficial passivating film of titanium oxide it has excellent corrosion resistance. On the other hand, nickel is one of the essential trace elements. Low nickel offers reduce growth, leads to anemia, arakeratosis-like damage and increased perinatal mortality [49]. Too high nickel concentration in vitro showed toxic effect with cellular damage [50] and nickel implanted intramuscularly or inside bone causes adverse tissue reactions such as local tissue irritation, necrosis

and toxic reactions [51]. Nickel could lead to carcinogenesis, however, cancer is very rarely associated with clinical implants and most occurrences (> 80%) have been related to cobalt-chromium alloy implants [52].

The study by Wever et al.[53] demonstrated in a test programme according to ISO 10993 (Biological evaluation of medical devices) [54] that Nitinol has no cytotoxic, allergic or genotoxic activity. Usually, the corrosion resistance of metal alloys is based on the creation of a metal oxide layer on the surface, which starts the passivation phenomenon. In the specific case of Nitinol, the surface is mostly composed of titanium dioxide (TiO₂), smaller amounts of nickel oxide (NiO and Ni₂O,) and nickel (Ni), while nickel-titanium alloy constitutes the inner layer [48], [55]. The biocompatibility of Nitinol has been investigated in many reviews and most studies suggest that the alloy has low cytotoxicity and low genotoxicity [56]. However there are discrepancies in the results obtained in different studies. The variation in corrosion resistance is generally attributed to the various surface state and chemistry, such as: surface roughness, inhomogeneities, sterilization processes, and polishing techniques [41], [55], [57]. Smooth surfaces with controlled chemistry of the external state of titanium dioxide are associated with negligible release of nickel ions, with concentrations below the normal human daily intake [56].

2.2.1.4. **Materia behavior in finite element analyses**

Many material models have been created to simulate the behavior of Nitinol in FE simulations. The model most used to simulate superelastic behavior is the one proposed by Auricchio and Taylor [58], [59]. The model is based on the uniaxial stress-strain response of those materials, such as Nitinol, which are in the austenitic phase under no load. When the material is loaded, after a certain stress, the stress induced transformation occurs and the austenitic phase begins to transform into martensite. Both martensite and austenite are assumed to follow isotropic linear elasticity [60].

When the phase transformation is completed the deformation follows the elastic constants of martensite, otherwise, the elastic properties are calculated from the elastic constants of austenite and martensite, following the rule of mixtures:

$$E = E_A + \zeta(E_M - E_A) \quad (1)$$

$$\nu = \nu_A + \zeta(\nu_M - \nu_A) \quad (2)$$

where E_A is the Young's modulus of austenite, E_M is the Young's modulus of martensite, ν_A is the Poisson's ratio of austenite, ν_M is the Poisson's ratio of martensite and ζ is the fraction of martensite [60].

During unloading, the martensite transforms back into austenite and the deformation is completely recovered. However, the stress at which the inverse transformation occurs is different

from the stress at which the direct transformation occurs, therefore the isothermal stress-strain behavior, up to the elastic strain limit of the material, under loading and unloading regime follows a hysteresis curve (Figure 2-5). According to the model, the hysteresis curve is characterized by four critical points: start and end stress values for the forward phase transformations from austenite to martensite (σ_{tL}^S and σ_{tL}^E respectively) and start and end stress values for the reverse phase transformations from martensite to austenite (σ_{tU}^S and σ_{tU}^E respectively).

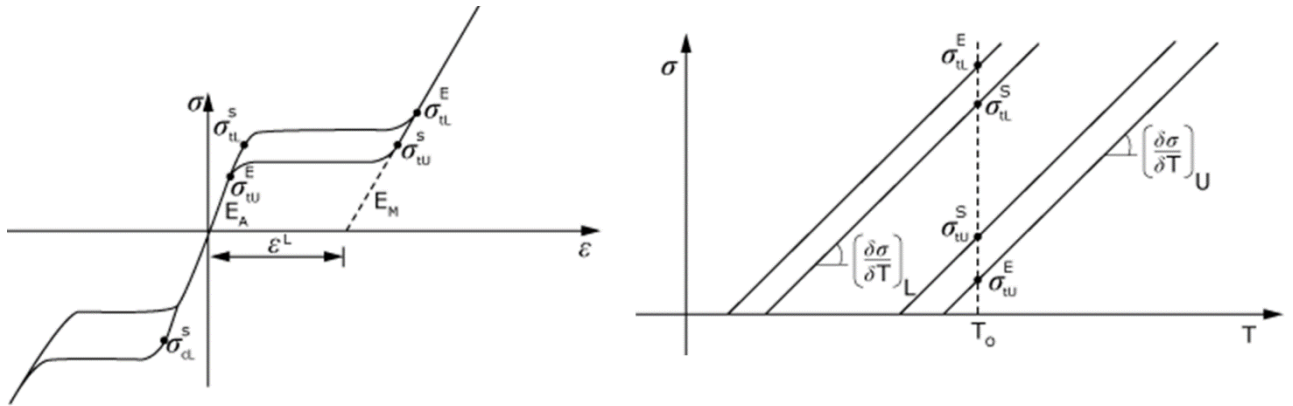


Figure 2-5: Superelastic behavior based on the uniaxial tension test and parameters for the definition of the material model. Graph adapted from [60].

2.2.2. Devices on the market

There are currently four IINI on the market: Smart Toe II™ (Stryker®), X-Fuse™ (Stryker®), Hmmerlock™ 2 (DePuy Synthes®) and Super Scaffold™ (Metric®).

- i. Smart Toe II is indicated for small bone reconstruction limited to inter-digital fusion of fingers and toes and small bone fusion [27]. It is designed to prevent rotational, sagittal, and transverse plane movements at the PIP joint to diminish the chance of recurrent deformity [61]. The device is made of body temperature activated shape memory Memometal Nitinol. It must be stored below 0 °C for two hours prior to surgery and when inserted, as the implant returns to its original shape, the proximal and distal leg expand (up to 3 mm) thus causing implant length reduction (up to 2 mm) which results in compression at the arthrodesis site [61][27]. There are different sizes ranging from 15 to 22 mm, all available in two angulation options: 0° (neutral) or 10° (angled). The size of the implant is chosen according to the dimensions of the proximal phalanx and middle phalanx and usually the angled option is chosen when the deformity is severe and the neutral option when the deformity is mild or moderate [6].

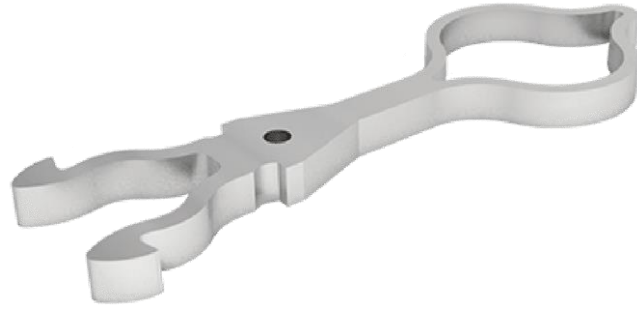


Figure 2-6: Smart Toe II. Picture adapted from [27].

- ii. Hammerlock 2 provides interfragmentary compression and active fixation without the need to freeze prior to usage. Indicated for small bone reconstruction and fusion such as in the phalanges of the fingers and toes [62], it gives the surgeon a means of intramedullary bone fixation and helps in the management of reconstructive surgery [29]. Unlike Smart Toe II, it can also be used in hand surgery and the Nitinol alloy used does not require storage at 0 °C before the implant because it uses the superelastic property of nitinol and not only the shape memory effect. It is inserted in a spear-like shape that allows it to fit in narrower proximal canals and once released it expands to provide multi-axial active stabilization [62]. As for the Smart Toe II, it is available in several sizes (17, 20, 22 mm) and in the straight or 10 ° angled version.



Figure 2-7: Hammerlock 2. Picture adapted from [29].

- iii. X-Fuse Memometal Nitinol implant is developed for small bone fusion, and more specifically for DIP and IP arthrodesis. It is a one piece implant with a flat design that resists rotation for control of the arthrodesis position. It is mainly used in hand surgery and it has four size options: small, standard, large and x-large (12.5, 15.5, 16.5, and 19.5 mm long respectively) and it is available in three angulations: 0°, 15° and 25°. The H-shaped design features two proximal legs and two distal legs. Before the implant, the legs are compressed by a clamp. Once implanted the clamp is removed and the device expands into the bone thanks to the superelasticity of Nitinol [26].



Figure 2-8: X-Fuse. Picture adapted from [26].

- iv. Super Scaffold is a hollow fenestrated cylinder implant fabricated from nitinol alloy with a section that increases its diameter (from 2.5 to 7.5mm) while shortening its length. The cylinder's surface has a feature that locks it into the bone with a force up to 9.6 N. The implant is retained in an instrument, advanced into the bone and released so that the elastic properties of nitinol will cause its diameter expansion and length shortening. It is designed to expand and lock into the intramedullary space and pull together and compress bone as the device shortens. It shortens 3 mm and applies up to 27.1 N compression force. The device is constrained to the bone and shortening may not occur, in this case, the compressive force at the bone interface is maximal and the potential shape change may pull the bone segments together if bone interfacial resorption occurs. It is used in both hand and foot surgery [28].



Figure 2-9: Super Scaffold. Picture adapted from [28].

2.2.3. Device design

The choice of the geometry, together with the material used, is a key element when designing the nail. Even the smallest variations lead to significant alterations in performance. In fact, IINIs have a completely different geometry compared to K-wires, because they aim to overcome the limitations to which a filiform design is subject.

A research regarding all the papers published about IINIs was performed using the search engines PubMed and Google Scholar and as keywords the name of the devices currently on the market. Only publications concerning Smart Toe (later purchased by Stryker® and improved as Smart Toe II) and X-Fuse were found. Several studies have been conducted with the aim of comparing the performance of the Smart Toe system against the K-wires standard. Angirasa et al. [63] installed 13 Smart Toe implants and 15 k-wires. All the Smart Toe implants achieve end-to-end complete arthrodesis while 40% of K-wires did not. Obrador et al. [64] reported that 10.6% of the 94 Smart Toe implanted broke during the first year while no single breakage occurred for the 65 K-wires used. Moreover, they found statistical differences in the degree of fusion across toes treated with a K-wires (35.4% non-unions) compared to Smart Toe (3.2% non-unions). Scholl et al. [15] implanted 58 Smart Toe and 28 K-wires: osseous union was achieved in 68.9% of Smart Toe devices and 82.1% of buried K-wires; revision surgery or fixation removal occurred in 8.6% of Smart Toe devices and 10.7% of K-wires. On the other hand, fracture of internal fixation occurred in 20.7% of the Smart Toe implants and 7.1% of the buried K-wires. Ferrier et al. [65] evaluated and compared clinical improvement, radiologic fusion, and complication rates between 69 Difuse™ (a dynamic IINI no longer on the market from Biotech Ortho) and 97 static TinyFix™ implants from Biotech Ortho, reporting that fusion rate was lower in dynamic implants compared to static implants (67% vs 80% respectively), osteolysis was more frequent in Difuse (12% vs 4% respectively), implant fractures were noticed in 4% of Difuse implants and the percentage of patient complaining pain at the last follow-up was 3% for Difuse and 7% for TinyFix.

Comparing the gold standard with new devices is useful for understanding how design variations lead to different clinical outcomes. However, one of the aims of this work is to develop a framework to assist the design process to improve product quality, therefore it is of fundamental importance understand which are the current problems that most afflict the devices on the market. For this reason, an analysis of all the complications regarding IINI reported in the literature has been performed. From the review conducted has emerged that there is a risk of implant migration and that the complications due to the breakage of the Smart Toe implantable device are not negligible (Table 2-2).

Table 2-2: Literature review of the main complications reported. Complication rates are expressed as a percentage and number of events over total.

IINI model	Study information's			Complications		
	Authors	Study design	Number of implants	Non-union	Implant breakage	Implant migration
Smart Toe	Cuttica et al. [66]	-	32	3.1% (1/32)	6.2% (2/32)	3.1% (1/32)
	Delmi et al.[67]	prospective	170	1.8% (3/170)	1.8% (3/170)	0.0%
	Angirasa et al.[63]	retrospective	13	0.0%	0.0%	0.0%
	Obrador et al.[64]	retrospective	94	3.2% (3/94)	10.6% (10/94)	0.0%
	Scholl et al.[15]	retrospective	58	31.0% (18/58)	20.7% (12/58)	0.0%
	Khan et al.[68]	prospective	82	3.7% (3/82)	2.4% (2/82)	0.0%
	Sandhu et al.[14]	retrospective	65	6.2% (4/65)	3.0% (2/65)	1.5% (1/65)
	Roukis et al.[69]	retrospective	30	7.0% (2/30)	0.0%	0.0%
	Payo-Ollero et al.[6]	prospective	50	2.0% (1/50)	8.0% (4/50)	0.0%
	Catena et al.[61]	prospective	42	-	4.8% (2/42)	2.3% (1/42)
X-Fuse	Jakubek et al. [70]	prospective	41	5% (2/41)	0.0%	0.0%
	Seitz et al.[5]	-	32	3.0% (1/32)	0.0%	0.0%
	Savvidou et al.[4]	prospective	7	14.0% (1/7)	0.0%	0.0%
	Almeida et al. [71]	retrospective	54	11.0% (6/54)	1.8% (1/54)	0.0%
	Ameline et al.[72]	retrospective	38	5.2% (2/38)	0.0%	0.0%
Difuse	Ferrier et al. [65]	retrospective	69	-	4.4% (3/69)	0.0%

The overall rupture rate across all published IINI studies is 4.7% (41/877). The maximum rupture rate reported is 20.6% (12/58) by Scholl et al. [15]. Across Smart Toe implant, the rupture rate increases to 5.8% (37/636). Eight out of 10 studies reported at least one cases of Smart Toe breakage.

Scholl et al. [15] hypothesized that the rupture could be due to the improperly performed implant procedure. In particular, in the first phase, the implant could be pushed excessively into the

proximal phalanx leading to an increase in stress in the thin distal legs, with fracture as the final outcome. Fractures of the proximal legs, on the other hand, could be caused by implants too short or too long than necessary which might place more torque on the proximal legs. Subsequently Smart Toe was purchased by Stryker Osteosynthesis and Smart Toe II was created. The implantation technique has been improved thanks to a hole in the center of the device that allows the insertion of a temporary fixator that prevents the abovementioned migration into the proximal phalanx. Furthermore, Smart Toe II is available in a wider range of sizes reducing the risk of using an implant that is too large or too small.

From these reports emerges a relevant issue regarding the structural strength of IINIs and a not negligible risk of implant migration. These aspects can be addressed by focusing on the design phase with the integration of numerical methods for *in silico* simulations. When designing an innovative device like IINIs, there are many aspects to take into consideration. Pietrzak et al. listed the four main characteristics that a fixation implant should satisfy [73].

First, the implant must provide adequate biomechanical support. K-wires are an effective means to stabilize the PIP joint after joint resection. They stiffen the joint and are very resistant, this is also proven by the low breaking rate. On the other hand, the first IINI showed significant critical issues in terms of geometry design and mechanical properties which resulted in a significant implant failure rate. Over time and experience, product design has improved and measures have been taken to improve biomechanical support. Certainly, the critical points on which attention must be paid during the design are the correct dimensioning of the components to avoid breakage due to loads higher than those expected. Attention should be paid also in creating a geometry that prevents the migration of the implant by means of anchors and contact forces, generated by the variation of the geometry, sufficient to keep the device well adhered to the bone.

Second, the complication profile must be acceptable. IINIs were created specifically to reduce the complications resulting from the use of K-wires. In particular, the complications due to an object passing through the protective barrier of the skin and the risks related to the exposure of a double surgery. Despite this, complications related to IINI must be monitored, with particular attention to the risk of breakage and migration of the device. Furthermore, there are no studies regarding the newest devices, therefore it is difficult to monitor the most common complications.

Third, the device must be convenient for the surgeon to implant and the patient to manage. The procedure for inserting most of the IINIs is easily performed by the orthopedist. It is sufficient to prepare the joint area and drill the distal and proximal phalanx in order to be able to implant the device within both.

Fourth, the implant should be cost-effective. Costs include the price of the device and surgical tools, direct medical costs, lost wages, and intangible costs such as the pain experienced by the patient and time spent during hospitalization and follow-up. Coillard et al. [74] reported a 20 times higher price of IINI compared to the K-wire. As previously described, the reported complications of IINI and K-wires have different rates depending on the clinical study considered. Someone report better performance with K-wires, others using IINIs. This leads to thinking that the performances are roughly comparable. Guelfi et al. [25] conducted a systematic review on the most recent publications regarding IINIs concluding that newer intramedullary devices provided good results, but the question is whether IINIs are more effective than traditional Kirschner and at the moment the increase in effectiveness does not seem to justify the significant increase in prices [25].

2.2.4. Regulation

The ASTM F1264 [75] is a standard for Intramedullary Fixation Devices (IMFDs) that specifies the test methods to achieve the certification.. This specification is intended to develop a standard which defines performance criteria and methods for measurement of performance related mechanical characteristics of IMFDs for surgical fixation of the skeletal system and their fixation to bone.

This specification includes four standard test methods:

- i. Static Four-Point Bend Test Method is intended to evaluate the bending strength or bending stiffness of the working length of the IMFD. However, this test method is designed specifically for IMFD that have a well-defined working length of uniform cross-section throughout the majority of its length and shall be applied to the full length of the diaphysis of a femur, tibia, humerus, radius, or ulna. Therefore, as the ASTM standard mentions, "This is not applicable to IMFDs that are used to fix only a short portion of the diaphysis of any of the long bones or the diaphysis of small bones such as the metacarpals, metatarsals, phalanges, and so forth."
- ii. Static Torsion Test Method covers the test procedure for determining the torsional stiffness of IMFDs and requires a straight section of IMFD with an approximate length of 28 cm. Therefore it does not apply to IINIs.
- iii. Bending Fatigue Test Method is intended to evaluate the cyclic bending fatigue performance of the working length of the IMFD. Similar to the Static Four-Point Bend Test Method it is related to IMFDs that are indicated for surgical fixation of the skeletal system and are typically used in the femur, tibia, humerus, radius, or ulna.
- iv. Test Method for Bending Fatigue of IMFD Locking Screws which is specifically applicable to screws described by Specification and not to IINIs.

Although there is a standard for testing IMFD, it is not possible to apply it to the specific case of IINIs due to their variable cross-section along the working length, small size and specific field of use in the phalanges. Therefore, there currently no standard for testing IINIs. The tests to evaluate the biomechanical behavior of an IINI were defined in this thesis. Four criteria were followed during the conceiving: the tests must be universal and appropriate for all IINIs, must be reproducible experimentally, must have a low computational cost and provide useful information to achieve the set objective. In addition, experimental tests previously performed on interphalangeal intramedullary nails [73], [76] were also considered.

To date, only two experimental studies have been conducted on intramedullary nails for phalangeal arthrodesis. To compare the mechanical properties of two types of interphalangeal intramedullary devices, Pietrzak et al. [73] created an experimental study simulating the clinical use of the implants. The implants were inserted into two blocks of synthetic bone to reproduce the joint formed by the two phalanges. A curved interface between the two blocks was used to provide freedom of movement. This way, the stability afforded by the implant can be tested without the influence of the wedge-opening. The wedge-opening effect is caused by a flat interface and could augment the stability of the construct. The proximal block was fixed with a gripping device, while a load was applied to the distal block at a distance of 19 mm from the contact interface between the two blocks in order to move downward at the rate of 12.7 mm/min (Figure 2-10).

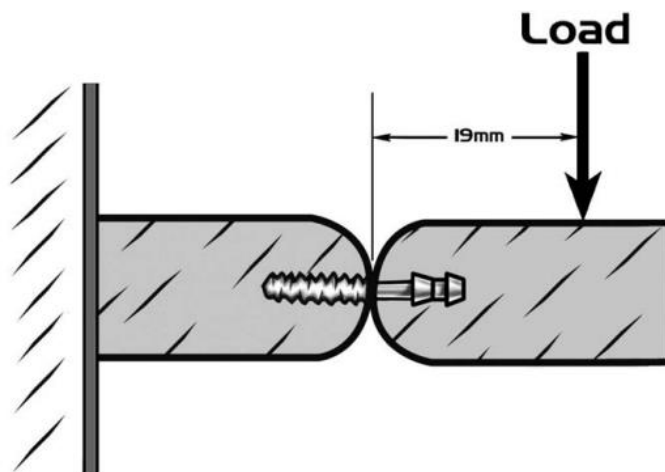


Figure 2-10: Schematic of a sagittal cross-section showing implant providing fixation for the bone block and load conditions. Figure adapted from [73].

Rothermel et al. [76] used an experimental approach similar to the previously described to compare two IINIs, X Fuse and Smart Toe, with the K-wire fixation gold standard. The aim was to evaluate which implant provides a stronger and stiffer arthrodesis construct. They conducted a biomechanical cadaveric study by inserting the implants into bones of phalanges. All proximal specimens were rigidly fixed and oriented facing upwards at approximately 12 degrees and the

actuator's load cell was aligned 7 mm away from the PIP joint in the distal phalanx. (Figure 2-11). Specimens were cyclically loaded in stepwise fashion at 1 Hz. The extension bending force of the PIP joint mimicked the natural upward bending force in walking using 2 N step increases of force with 10 cycles per step starting from a compressive force of 2 N.

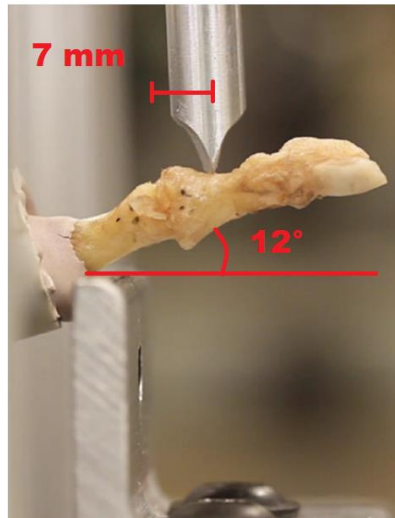


Figure 2-11: Specimen preparation after implantation of K-wire, X Fuse, or Smart Toe device. The toe was aligned oriented facing upwards at 12 degrees and secured to a custom jig with the loading pin wedge aligned 7 mm away from PIP joint. Picture adapted from [76].

2.2.5. State of the art finite element analysis

The FE method is a numerical technique designed to seek approximate solutions to problems described by partial differential equations. It finds applications in structural analysis, mass transport, fluid flow, heat transfer, and electromagnetic potential. FE analysis enables to predict potential design issues and failures already during the design process, thus minimizing the experimental testing costs and improving the quality of the product.

Up to now, the only work regarding FE analysis of an IINI was conducted by Bayod et al. [77]. They evaluate the reduction of dorsal displacement of the toes phalanges during the push-off phase of gait after the implantation of a Smart Toe implant, used for proximal interphalangeal joint arthrodesis. Within this work the CT scan of a foot was semi-automatically segmented distinguishing cortical and cancellous bone for each of the 28 bones that compose the foot. The meshes of the bones were then connected through cartilage joints and ligaments, modeled with a set of 483 incomprehensible one-dimensional elements (Figure 2-12).

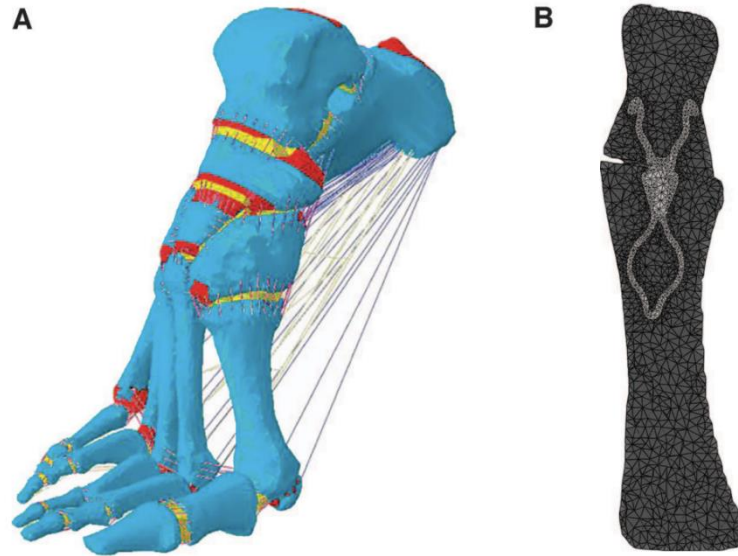


Figure 2-12: (A) FE model of the foot: bones, cartilage, ligaments, plantar fascia, flexor digitorum longus and flexor digitorum brevis. (B) Mesh of the neutral implant embedded in the second phalanx. Picture adapted from [77].

Smart Toe, neutral and angled version, implant was scanned in three dimensions, and the mesh was inserted into the finite element model of the phalanges. Implants were modeled as a linear, elastic material, with a Young modulus of 110'000 MPa, a Poisson coefficient of 0.33, and a tensile yield strength of 430 MPa. The Push-off phase was reproduced by applying a normal load of 180 kg to the surface formed by the contact of the tibia and the fibula with the talus and a load of 12 kg tangent to the surface. Finally, they found a greater reduction in maximum displacement for all of the planes when using the neutral implant compared with the nonsurgical foot as well as when comparing angled implant with the nonsurgical foot except for the lateromedial displacement in the PIP and MTP (Figure 2-13).

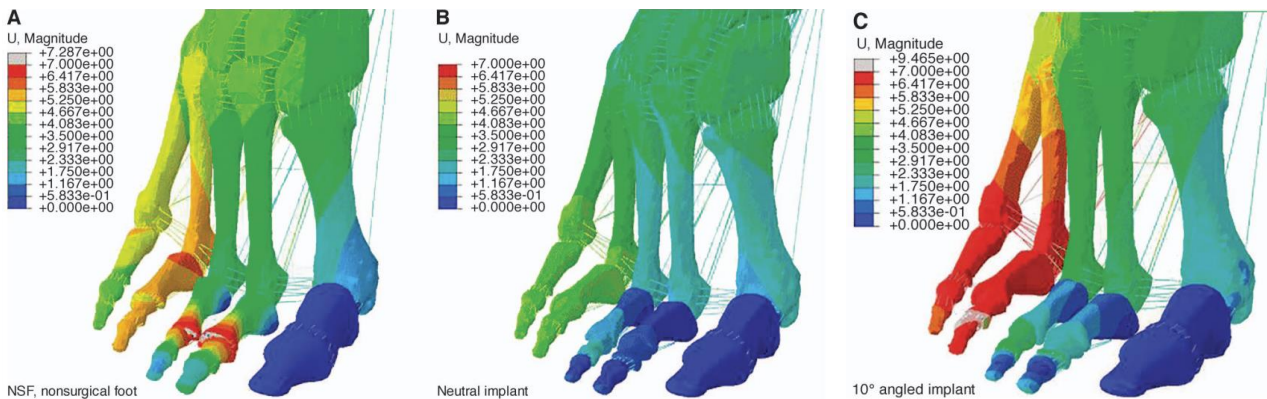


Figure 2-13: Displacements in the three planes in millimeters in case of: (A) no intervention performed; (B) PIP joint arthrodesis performed using a simulated neutral implant placed at the second to fourth toes; (C) PIP joint arthrodesis performed using a 10° simulated angled implant at the second through fourth toes. Picture adapted from [77].

The study focuses only on the effects that the implant produces on the foot, it does not evaluate the effects that the movements and the intersegmental forces of the foot have on the IINI. Furthermore, the properties assigned to the implant material do not consider the superelastic behavior of Nitinol. Although numerous cases of device breakage have been reported, there is no study which analyses the structural integrity of the implants when subjected to physiological or unexpected loads. FE studies could improve the safety and efficacy of IINIs by examining their biomechanical behavior *in vivo*.

3. Materials and Methods

Currently, there are four IINIs available on the market, see 2.2.2. Each of them is characterized by different geometries that allow the anchoring to the bone and to bring the phalanges closer to promote fusion. This work focuses on the Smart Toe II implant. Numerous studies [6], [14], [15], [61], [63], [64], [66]–[69] have been carried out on Smart Toe to evaluate its performance and, as described in paragraph 2.2.3, some critical issues have also been identified regarding its structural failure rate and implant migration. A new device, Smart Toe II, has now been developed in order to solve the issues emerged from clinical studies. The FE analysis carried out in this work has been performed on a three dimensional model that reproduce the Smart Toe II geometry.

As described in paragraph 2.2.1.1, the two peculiar properties of nitinol are shape memory effect and superelasticity. IINIs can be divided into two categories depending on the properties of the Nitinol they exploit. The nails which exploit the shape memory effect are composed of an alloy that has A_f slightly lower than the body temperature and higher than the room temperature. Accordingly, the device changes spontaneously its geometry after being implanted, thanks to the heat released by the body. The nail, switches from the compact shape, maintained during storage and just before the implant, to the expanded nail shape, reached when heated to body temperature. Usually these devices must be stored at 0 °C a few hours before use. The nails which exploit superelasticity, are composed of an alloy that has a lower A_f than the ones described above. At room temperature the nail is already in the expanded form. Therefore, the surgeon uses a tool to elastically deforms the device in the compact shape. When the device is implanted, the tool that constrains the nail expansion is removed and the implant is free to return to its original shape and anchor to the bone.

Smart Toe II exploits shape memory effect, in fact it must be kept in the freezer at least two hours before implantation. However, once implanted, the body temperature is higher than the temperature at which the transformation to austenite ends ($T > A_f$). Therefore, the device exploits superelasticity. Smart Toe II when inserted into the body behaves like those nails which exploit superelasticity and require a tool to prevent expansion. The only difference is that in this case the complete expansion of the implant is prevented by the bone.

To simplify the prototyping process and lighten the simulations the framework developed in this work is based on submodeling. Submodeling is the technique of studying a portion of a larger model in order to get more specific information. The method is used to obtain an accurate, detailed solution in a local region when the detailed modeling of that local region has a negligible effect on the overall solution [78]. The global model is used to establish the boundary conditions of the

submodel and in this case with “boundary conditions” it is meant literally conditions at the boundary of the submodel.

3.1. Geometrical model

The three-dimensional geometrical model of the Smart Toe II implant was created on the basis of the drawings, photos and measurements publicly available in papers and datasheet. An overhead photograph of the device [Figure 3-1 (a)] was scaled using the measurements documented on datasheets [27] and used as a basis for the realization of the model. SolidWorks 2020 (SolidWorks Corporation, Waltham, MA, USA) was used to create a parametric model of the geometry.

In particular, the geometry of a 10 ° angled Smart Toe II model with a length of 22 mm was reproduced. The device can be divided into two parts: the proximal part, inserted in the proximal phalanx, which has the shape of a flattened ring and the distal part, inserted in the distal phalanx, consisting of two curved legs, which end with a hook facing outwards. [Figure 3-1 (b)]. When the device is positioned with the proximal part parallel to the horizontal plane, the distal angled part is directed downward. There is a hole that divides the proximal part from the distal one. Through that hole the surgeons can insert a pin to check that the implant is well-positioned between the two adjacent phalanges, to prevent implant migration when the two phalanges are approached.

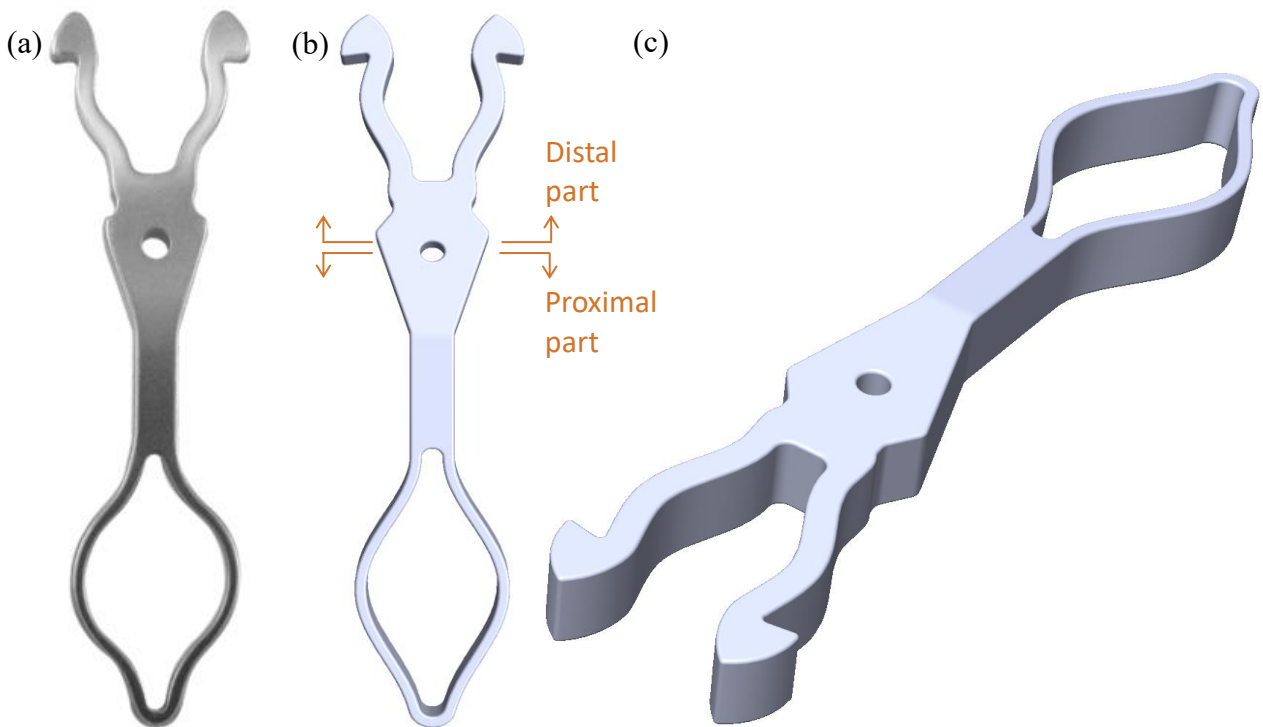


Figure 3-1: (a) Overhead photograph of a real Smart Toe II device. Photo adapted from [27]. Top view (b) and perspective view (c) of the created three-dimensional model of Smart Toe II.

3.2. Finite element model

A tetrahedral volumetric mesh C3D4 was created using Hypermesh (Altair Engineering, Troy, MI, USA). A total of 69'799 nodes and 372'704 linear tetrahedral elements of type C3D4 were created. The choice of the tetrahedral mesh was conducted to obtain a good representation of the complex geometry. The mesh has a variable size to optimize the computational cost, with smaller elements at the fillets and curvatures and gradually larger elements elsewhere. The average element size is 0.065 mm.

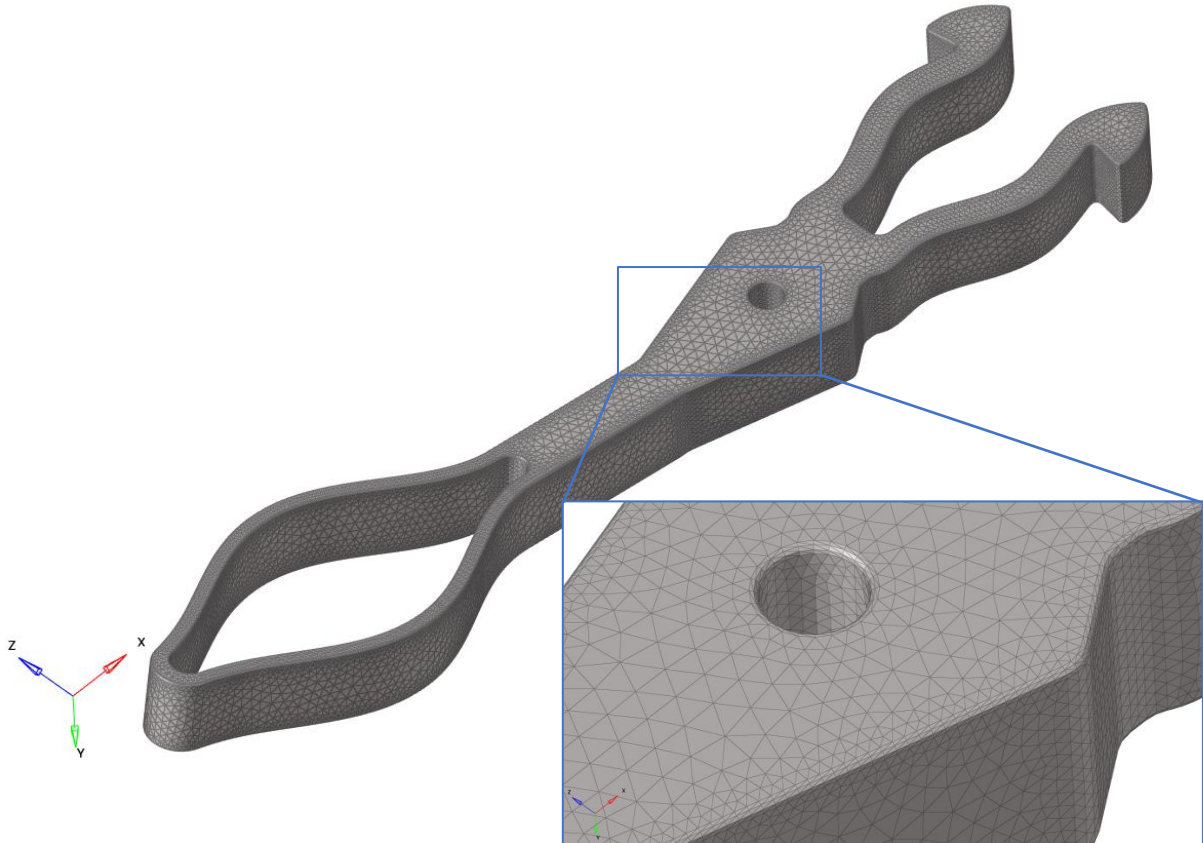


Figure 3-2: Mesh created on the three-dimensional model of the Smart Toe II and enlarged detail to appreciate the size variation of the elements.

The material property was then assigned to the model. As mentioned before, once implanted, Smart Toe II can be considered as those IINIs that exploit superelasticity. Therefore, in the simulations, a superelastic model of the material was used. Specifically, an Abaqus user-defined material subroutine (UMAT) based on the work of Auricchio and Taylor [58], [59] was used to simulate the superelastic behavior of Nitinol (see paragraph 2.2.1.4).

Abaqus *ELASTIC option was used to define the Young's modulus and Poisson's ratio of austenite. *SUPERELASTIC option was used to define the elastic properties of martensite, the critical stress levels for forward and reverse transformation, and the variation of transformation

plateau with temperature. *DENSITY option was used to define the density of the material. In Table 3-1 are reported the material parameters used in FE analysis of this work.

Table 3-1: Material parameters. From [79]

Symbol	Description	Value
ρ	Density	6500 Kg/m ³
E_A	Young's modulus of austenite	63000 MPa
ν_A	Poisson's ratio of austenite	0.3
E_M	Young's modulus of martensite	63000 MPa
ν_M	Poisson's ratio of martensite	0.3
ϵ^L	Uniaxial transformation strain	3.25 %
σ_{tL}^S	Stress at which the transformation begins during loading in tension	420 MPa
σ_{tL}^E	Stress at which the transformation ends during loading in tension	500 MPa
σ_{tU}^S	Stress at which the reverse transformation begins during unloading in tension	360 MPa
σ_{tU}^E	Stress at which the transformation ends during loading in tension	280 MPa
σ_{cL}^S	Stress at which the transformation begins during loading in compression, as a positive value	495 MPa
T_0	Reference temperature	37 °C
$\left(\frac{\delta\sigma}{\delta T}\right)_L$	Slope of the stress versus temperature curve for loading	6.3 MPa/°C
$\left(\frac{\delta\sigma}{\delta T}\right)_U$	Slope of the stress versus temperature curve for unloading	6.3 MPa/°C

The material parameters implemented in the model should be obtained experimentally from a uniaxial tensile test of a Nitinol specimen equal to the one used in the analyzed device. The experimental test must be conducted at the reference temperature (37 ° C). From the curve in the stress-strain graph it is possible to interpolate the values of the five characteristic stresses (σ_{tL}^S , σ_{tL}^E , σ_{tU}^S , σ_{tU}^E and σ_{cL}^S) and calculate the initial and final slope of the curve to derive the austenite and martensite Young's modulus respectively. In this work, specimens of the material used in the studied implant were not available and material data from the literature were used. The same values of the material parameters interpolated by Subasi et al. [80] from the results of the uniaxial tests conducted by Saleeb et al. [81] on Nitinol specimens for orthopedic staples were used.

3.3. Finite element analysis

Two different simulations were conducted to evaluate the biomechanical behavior of the implant under *in vivo* conditions, by providing representative quantities of mechanical performance. The first test aims to reproduce *in silico* the push-off phase of gait. It provide stress-strain information in order to identify the most stressed areas and provide an estimate of the bending moment and displacement the nail can support. The second test evaluates the biomechanical behavior during nail expansion into the medullary canal. It allows to determine the contact forces between the bone and the implant and estimate the anchor force which are closely related to the risk of bone non-union and implant migration.

Abaqus/Standard solver (Dassault Systemes Simulia Corp., Providence, RI, USA) was used to perform the non-linear static analyses. The temperature was set at 37 ° C in all nodes and an artificial damping was used to stabilize the simulation.

FE analyses were performed on a workstation running Windows 10 Pro with Intel® Core™ i7-9700K 3.6 Hz processor and 32 GB of RAM.

Henceforth, it was considered a Cartesian reference system with the *xz* plane parallel to the ground and the *y* axis in a vertical and upward direction (Figure 3-3).

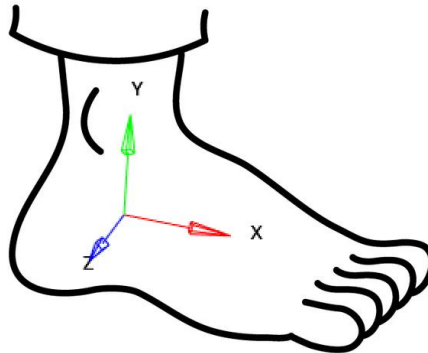


Figure 3-3: Cartesian reference system.

3.3.1. Model verification

In both simulations, stresses and strains were evaluated in order to verify that the material model was implemented correctly. The trend of the stresses as a function of the strains in the most stressed node was plotted. The stress-strain curves of the two simulations were compared with the curve of the implemented material model.

The distribution of stresses and strains in the device was critically observed. The results of the simulations were compared with the solution of the simplified analytical case. In the simulation of the bending of the device, the distal legs can be considered as a cantilever beam, blocked at the point

of insertion in the body of the device, to which a force orthogonal to the beam's axis is applied. In this case, the analytical solution to determine the stresses is given by the flexure formula:

$$\sigma = -\frac{M(x)y}{I} \quad (3)$$

where $M(x)$ is the bending moment at the location of interest along the beam's length x , $M(x) = Fx$, y is the distance from the beam's neutral axis to the point of interest along the height of the cross-section and I is the centroidal moment of inertia.

3.3.2. Bending of the implant

Smart Toe II is designed to be implanted between two adjacent phalanges and promote arthrodesis. Under certain operating conditions, the implant may bend around the z axis. This condition can occur during the push-off phase of the step, phase in which the device is most stressed. In this situation the proximal and distal phalanges, joined together by the device, hyperextend due to the high forces generated by the weight of the subject and the movement of the foot during the step.

The test conceived in this work aims to assess the mechanical performance of the device by simulating its bending during the push-off phase. The part of the implant intended to be inserted into the proximal phalanx was locked while the part intended to be inserted into the distal phalanx was loaded at a distance of 6.6 mm from the central hole (Figure 3-4).

The following boundary conditions were applied.

First step:

- The proximal part of the device was locked by imposing null displacements and rotations.

$$U_x, U_y, U_z = 0$$

$$\text{Rot}_x, \text{Rot}_y, \text{Rot}_z = 0$$

- On the inferior surface of each of the two hooks at the end of the distal legs, was applied an upward displacement in the y direction of 0.7 mm and a null rotation around the x axis. The displacement was assigned to two masters, each connected to the nodes of the surfaces of the two hooks, by means of rigid elements RBE2.

$$U_y = 0.7$$

$$\text{Rot}_x = 0$$

Second step:

- The proximal part of the device was locked by imposing null displacements and rotations.

$$U_x, U_y, U_z = 0$$

$$\text{Rot}_x, \text{Rot}_y, \text{Rot}_z = 0$$

- The masters, connected to the inferior surface of the hooks, were constrained to return to the initial position held at the beginning of the first step.

$$U_x, U_y, U_z = 0$$

$$\text{Rot}_x, \text{Rot}_y, \text{Rot}_z = 0$$

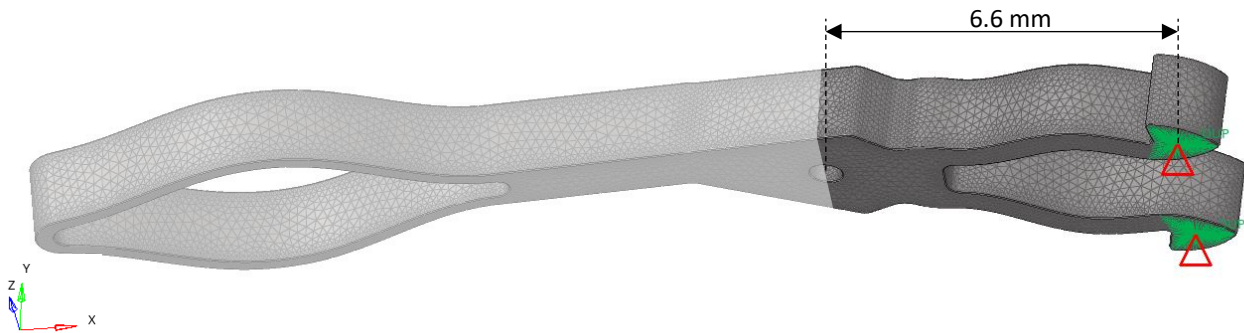


Figure 3-4: Schematic representation of the boundary conditions. In green the nodes to which the displacement has been assigned. The nodes locked in the proximal part are marked in light gray.

3.3.3. Fatigue assessment

IINIs are subjected to cyclic loads, therefore, it is important to evaluate the fatigue strength. Strong evidence of the importance of assessing fatigue is the Wöhler curve (Figure 1-1Figure 3-5). The curve is created as follows. An experimental test in which a large number of specimens are stressed to a given amplitude is performed, and the number of cycles they undergo before breaking is noted. The specimens will break following a normal distribution and the average value of the number of cycles before failure is calculated. The experimental test is repeated again and again on other specimens by varying the amplitude of stress, and the average value of the number of cycles before breaking is reported for each test. The graph is obtained by plotting on the x axis the number of cycles before failure and on the y axis the stress amplitude, and joining the points with a curve. The result will be similar to the one in the figure.

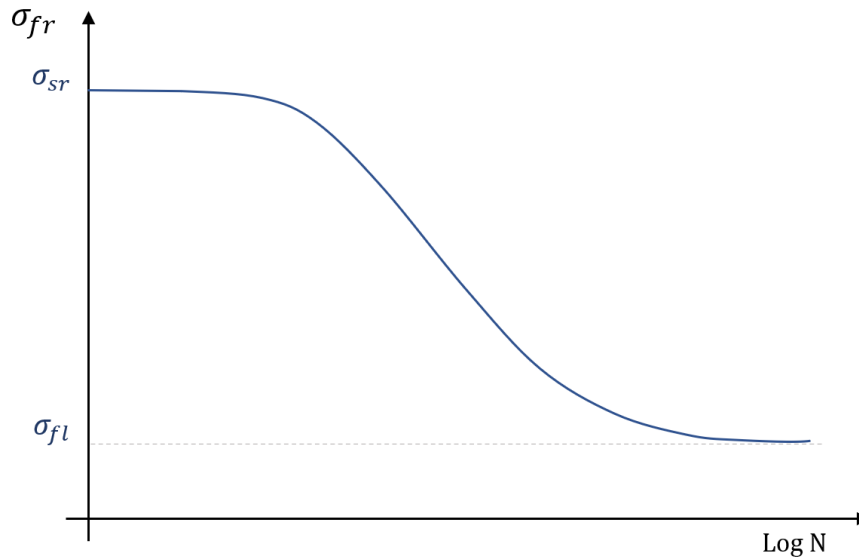


Figure 3-5: Example of a Wöhler curve. σ_{fr} = fatigue rupture stress; σ_{sr} = static rupture stress; σ_{fl} = fatigue limit stress; N = number of cycles.

The curve that joins all the mean values at each stresses is the Wöhler curve with a 50% probability of failure. In other words, the probability that a specimen subjected to a load stress of amplitude σ will fail before reaching the number of cycles delimited by the Wöhler curve is 0.5.

From the curve it is evident that as the number of cycles increases, the fatigue rupture stress is significantly inferior to the static rupture stress. For a number of cycles equal to one, the corresponding rupture stress σ_{fr} is equal to the static rupture stress σ_{sr} . Furthermore, the curve has a horizontal asymptote which tends to a stress value called the fatigue limit, below which the device can withstand an infinite number of cycles without breaking.

From the procedure for determining the Wöhler curve, can be deduced that fatigue tests are generally time consuming and require a large number of specimens. Therefore, being able to study fatigue strength via *in silico* simulations can make a difference in the design process of a new device.

To evaluate Nitinol fatigue strength in the literature are reported several methods, but the strain-based constant life diagram approach is the most commonly used criterion due to its simplicity. This uniaxial approach defines a safety threshold in terms of mean strain and strain amplitude for a given shape memory alloy (SMA) material and a specific number of cycles. But its uniaxial nature makes difficult the extension to multiaxial loading conditions [82]–[84].

The Dang Van criterion has been proposed by Auricchio et al. [85] to addresses the fatigue analysis of SMA under elastic shakedown. It has the advantage of being multiaxial and of taking into account the complexity of the phase transformation between austenite and martensite. According to

the criterion the device subjected to cyclic loading has an infinite lifetime if, for all points x of the structure:

$$\max_{t>t_0} \{ \hat{\tau}(\mathbf{x}, t) + a(\alpha(\mathbf{x})) \hat{\sigma}_h(\mathbf{x}, t) \} \leq b(\alpha(\mathbf{x})) \quad (4)$$

Where $\hat{\tau}$ is the mesoscopic shear stress, $\hat{\sigma}_h$ is the mesoscopic hydrostatic stress and a and b are parameters depending on α , which is the martensite volume fraction, that can be derived from two uniaxial fatigue experiments in tension and/or torsion.

Therefore if the condition is not respected the device will have a finite lifetime.

The linear inequality (4) splits the graph shear stress versus hydrostatic stress by a straight line for each α below which the lifetime of the device will be infinite. See Figure 3-6 as example. For a fixed number of cycles to failure N there are a set of Dang Van lines depending on the martensite volume fraction.

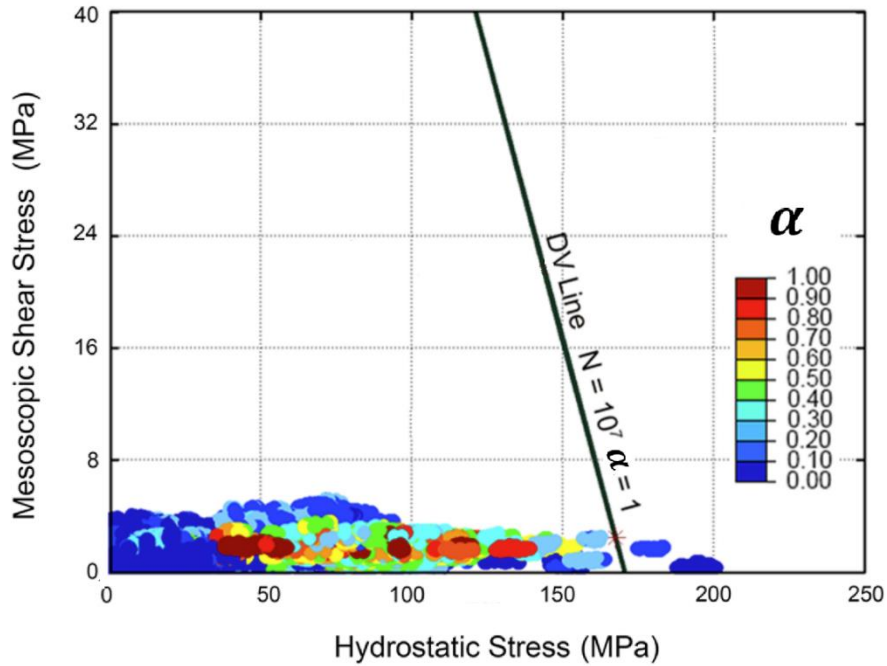


Figure 3-6: Dang Van diagram in terms of mesoscopic shear stress and hydrostatic stress for a stent device in Nitinol. The colored dots represent the stress paths of each integration point x of the device. The color scale indicates the martensite volume fraction α . The Dang Van line calculated for $\alpha = 1$ is marked in black. If the stress paths of the integration points having $\alpha = 1$ cross the Dang Van line indicates the failure of the device and an endurance limit lower than 10^7 cycles. In the example, the points that cross the line have $\alpha = 0$, therefore, no fatigue rupture occurs. Graph adapted from [84].

Scalet et al.[84] proposed a reformulation of (4). According to their formula for each point x a Dang Van fatigue damage parameter C_{DV} is calculated.

$$C_{DV} = \max_{t>t_0} \frac{\hat{\tau}(\mathbf{x}, t) + a(\alpha(\mathbf{x})) \hat{\sigma}_h(\mathbf{x}, t) - b(\alpha(\mathbf{x}))}{b(\alpha(\mathbf{x}))} \quad (5)$$

If it is positive it indicates a possible fatigue failure while if it is negative it indicates the absence of fatigue failure.

Since it was not possible to perform uniaxial experimental tests, it was not possible to derive a and b parameters, therefore, the strain-based constant-life approach have been implemented. The strain-based constant-life uniaxial diagram report the strain amplitude ε_a and the mean strain ε_m at a fixed number of cycles N for a certain material. In this case, similarly to the Dang Van method, in the diagram it is possible to identify a limit curve that discriminates whether the device will have an infinite lifetime. This curve is generally obtained from uniaxial experimental tests performed on classical specimens. Comparing the points in the ε_m - ε_a graph with the results obtained experimentally, it is possible to make considerations on the fatigue behavior of the analyzed device. If all the nodes lie below the limit curve, the device will not fail due to fatigue. Otherwise, if at least one point exceeds the curve, fatigue failure will occur.

The equivalent mean strain and strain amplitude can be evaluated in terms of maximum principal strain or in terms of the effective von Mises strain. In this work the strains were evaluated in terms of maximum principal strain. The equivalent mean strain and strain amplitude were calculated in each node using the following formulas:

$$\varepsilon_m = \frac{\varepsilon_{max} + \varepsilon_{min}}{2} \quad (6)$$

$$\varepsilon_a = \left| \frac{\varepsilon_{max} - \varepsilon_{min}}{2} \right| \quad (7)$$

Where ε_m is the equivalent mean strain, ε_a is the strain amplitude, ε_{max} is the maximum principal stress at the end of the first step of the bending simulation and ε_{min} is the maximum principal stress at the end of the second step of the bending simulation.

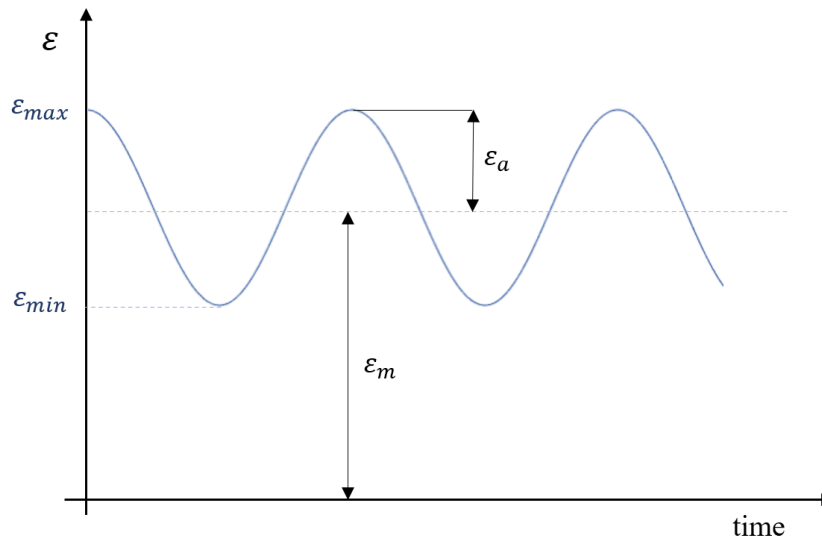


Figure 3-7: Representation of a cyclic deformation. ε_a = strain amplitude; ε_m = mean strain; ε_{min} = minimum strain; ε_{max} = maximum strain.

3.3.4. Expansion and anchoring of the implant

All IINIs exploits the superelasticity or shape memory properties of Nitinol to vary the geometry once inserted into the bone. The shape mutation allows the device to expand by increasing its cross-section (width) and adhere to the inner walls of the medullary canal in which it is inserted. At the same time, the shortening of the length allows to provide compression at the arthrodesis site. In Smart Toe II, the expansion of the nail occurs both in the distal and proximal part. The proximal part, a sort of flattened ring, when inserted into the bone, tries to return to its original shape with a wider lumen. The distal part, two small curved legs with a hook at the end, bend outwards (Figure 3-8).

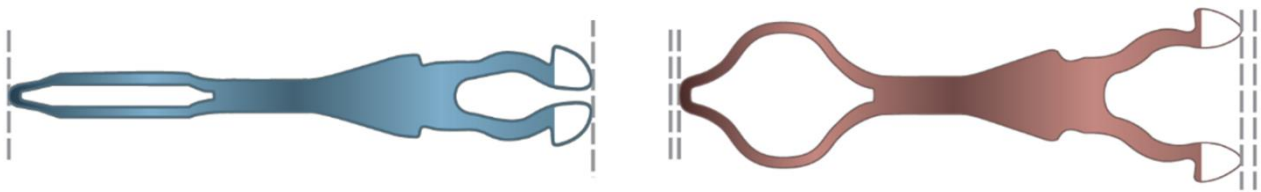


Figure 3-8: Schematic representation of the variation of geometry from the compact to the expanded configuration. Figure adapted from [27].

From the contact between the bone and the implant arise the contact forces which are responsible for anchoring the device to the bone. Therefore, it is important to be able to quantify these forces to predict the ability to adhere to the bone, manage the implant migration risk and control the compression in the joint and the phalanx rotation.

The FE simulation was structured as follows. Four rigid plates composed by SFM3D4R type elements were placed in correspondence of the areas where contact with the bone is expected. The contact between implant and plates was modeled by using the CONTACT PAIR algorithm with a friction coefficients equal to 0.1 [86]. The simulation was divided into two steps. In the first step, the implant was compressed to the compact nail shape (the shape it has before being implanted into the bone). To do this, the four plates were forced to move in the direction of the device until it was compressed into the desired shape (2.8 mm wide). In the second step, the plates were progressively removed from the device, which was able to resume its original form (expanded nail shape). The displacement of the plates was assigned to four masters, each connected to nodes of the four slave plates, by means of rigid elements RBE2 (Figure 3-9).

First step:

- The nodes belonging to the central part of the nail lying on the plane passing through the longitudinal axis of the device and parallel to the xy plane, have been locked by imposing null displacements and rotations.

$$U_x, U_y, U_z = 0$$

$$\text{Rot}_x, \text{Rot}_y, \text{Rot}_z = 0$$

- A positive or negative rigid displacement of 0.56 mm was imposed to the proximal plates depending on the reciprocal position between the plate and the device.

$$U_x, U_y = 0$$

$$U_z = 0.56 \text{ or } U_z = -0.56$$

$$\text{Rot}_x, \text{Rot}_y, \text{Rot}_z = 0$$

- A positive or negative rigid displacement of 0.93 mm was imposed to the distal plates depending on the reciprocal position between the plate and the device.

$$U_x, U_y = 0$$

$$U_z = 0.93 \text{ or } U_z = -0.93$$

$$\text{Rot}_x, \text{Rot}_y, \text{Rot}_z = 0$$

Second step:

- The nodes belonging to the central part of the nail lying on the plane passing through the longitudinal axis of the device and parallel to the xy plane, have been locked by imposing null displacements and rotations.

$$U_x, U_y, U_z = 0$$

$$\text{Rot}_x, \text{Rot}_y, \text{Rot}_z = 0$$

- The proximal and distal plates were constrained to return to the initial position held at the beginning of the first step.

$$U_x, U_y, U_z = 0$$

$$\text{Rot}_x, \text{Rot}_y, \text{Rot}_z = 0$$

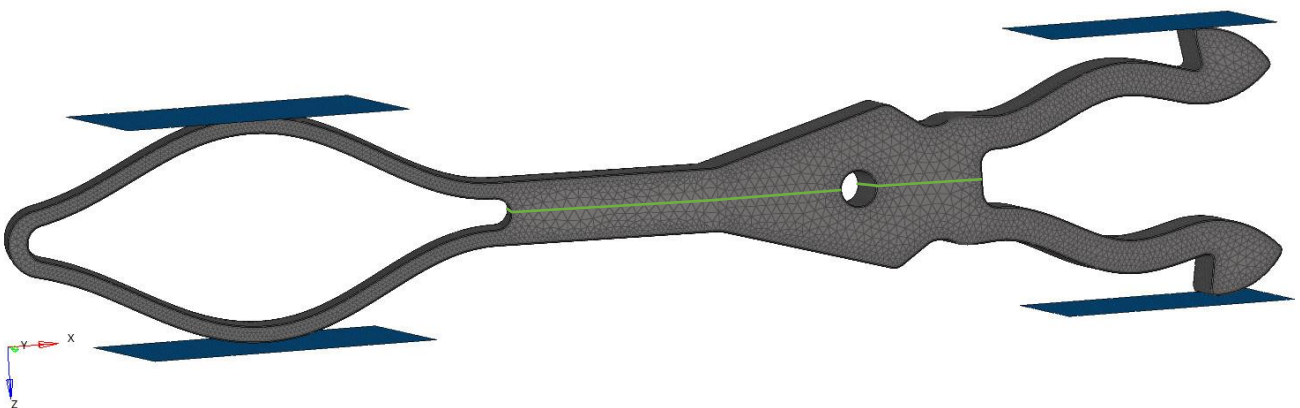


Figure 3-9: Schematic representation of the boundary conditions. In blue the plates to which a displacement has been assigned. The nodes locked are marked in green.

Using python scripts, nodal reaction force were evaluated in the four masters to estimate the contact force between the implant and the plates. The areas of the device in contact with the plates, during expansion, move mainly in z direction in both the distal and proximal part. Therefore, the contact forces were evaluated in the z direction, orthogonal to the contact surface.

The anchor forces are the friction forces between the nail and the bone. They were calculated multiplying the contact normal force by the coefficient of friction (COF) between the bone and the device:

$$F_{anchor} = COF \cdot F_{Contact} \quad (8)$$

The estimation of the friction coefficient should be performed in a laboratory by means of experimental tests. In this work, since experimental tests were not available, for purposes of example, the data published by Yangtao et al. [87] were used. They found that the fretting friction coefficient between Nitinol and human cortical bone is between 0.14 and 0.73. It should also be considered that the value of the coefficient varies considerably depending on the surface treatments of the material, the presence of lubricants and the type of bone. A coefficient of friction of 0.7 was used, which represents the rough surface of the internal bone canal.

4. Result

4.1. Model verification

The stress-strain curves in the most stressed node for the bending test and for the expansion test of the implant are shown in Figure 4-1 and Figure 4-2 respectively.

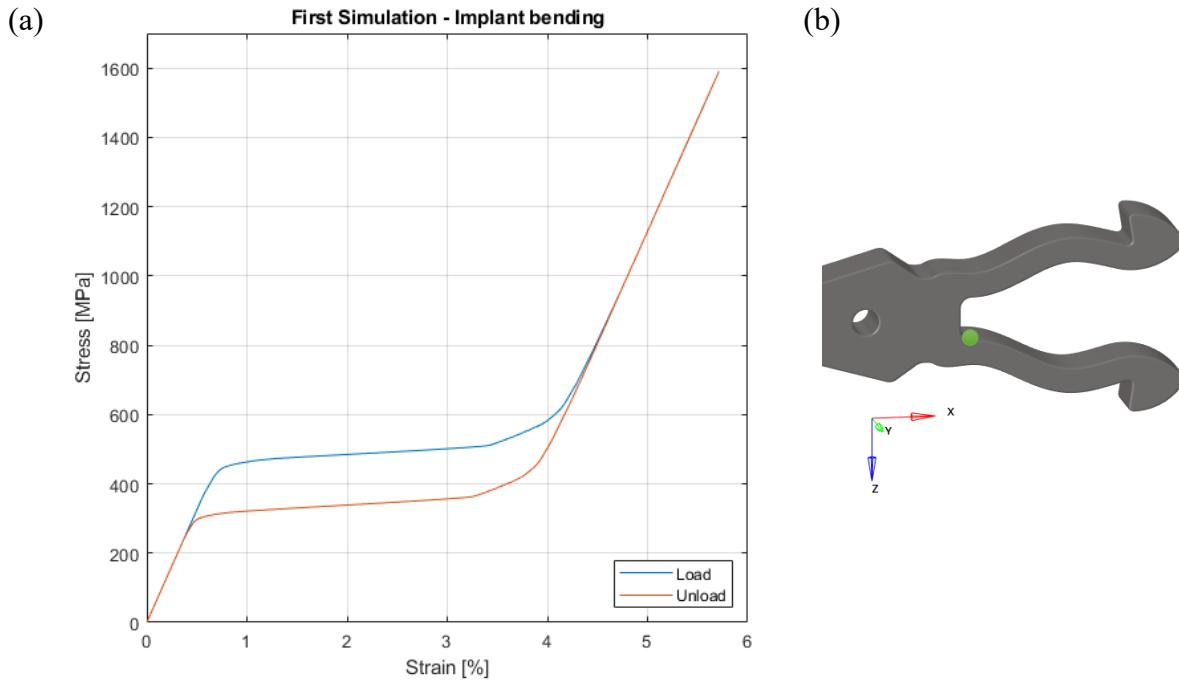


Figure 4-1: (a) Maximum principal stress–strain curve in the most stressed node during the bending of the implant. The curve obtained during the bending of the device (step 1) is plotted blue and the curve obtained during the return to the initial position (step 2) is plotted in red. (b) Position of the most stressed node, highlighted in green.

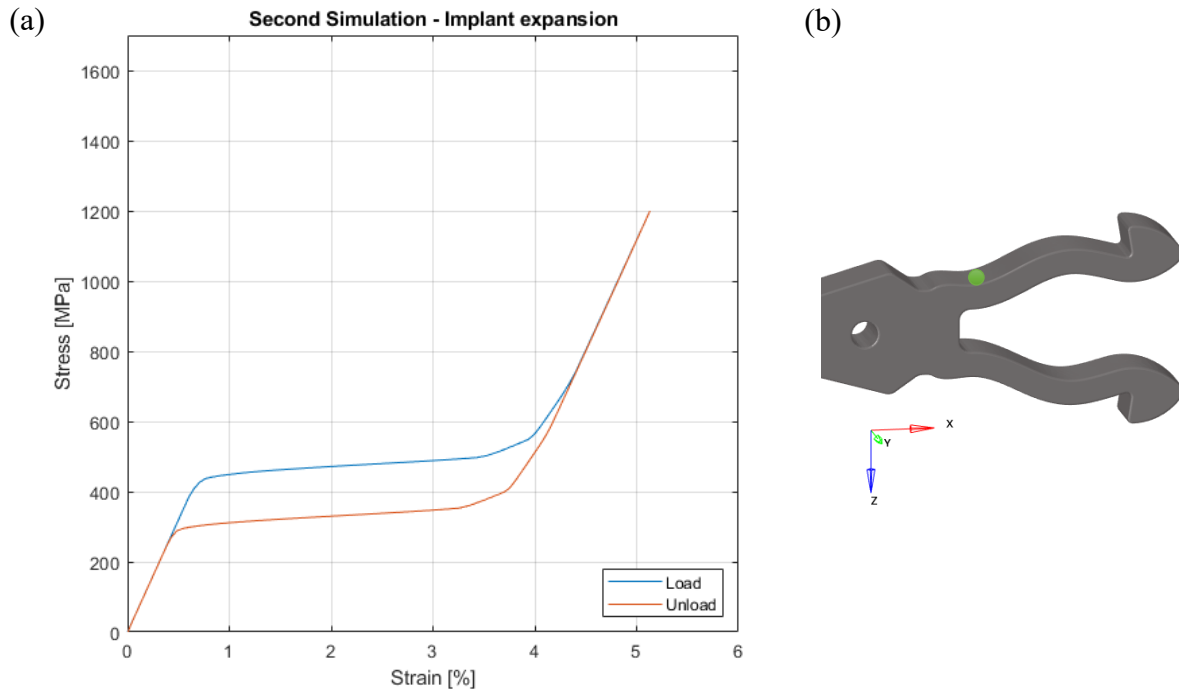


Figure 4-2: (a) Maximum principal stress–strain curve in the most stressed node during the compression and expansion of the implant. The curve obtained during the initial compression of the device (step 1) is plotted in blue and the curve obtained during the nail expansion (step 2) is plotted in red. (b) Position of the most stressed node, highlighted in green.

From the stress-strain graph it is possible to interpolate the values of the critical stresses. The Young's modulus of austenite and martensite were obtained by calculating the angular coefficient of the straight line in the first and last linear phases, respectively. Uniaxial transformation strain was calculated from the x-intercept of the line coinciding with the last linear phase of the martensite.

The analytical results of the cantilever beam are given by the flexure formula. According to the formula, the bending stress is zero at the beam's neutral axis and increases linearly away from the neutral axis until the maximum values at the extreme fibers at the top and bottom of the beam. Therefore, according to the analytical solution of a simple beam, the most stressed points are those at the top and bottom in the built-in end of the beam, where the force arm x and the distance from the beam's neutral axis y are greater. Moreover, the stress intensification factor increases as the radius of curvature of the surface decreases. Therefore higher stresses should be observed at the fillet and curvatures.

4.2. Bending of the implant

The analysis has been completed successfully and the computational time was 533 minutes (Intel® Core™ i7-9700K 3.6 Hz processor with 32 GB of RAM). After the simulation of the hypertension of the phalanges, the stresses and strains during the flexion of the device have been

observed. Strain and stress grow as the degree of flexion increases. The most stressed elements are located at the insertion of the legs in the body of the device, more precisely in correspondence with the upper and lower fillets in the internal part between the distal legs and in the external part at the first concavity of the legs. Compression stresses reach a peak of 1676 MPa in the upper area of the leg insertion. The maximum tensile stress is 1590 MPa in the lower area of the leg insertion (Figure 4-3). The maximum compression strain is 5.3%, while the maximum tensile strain is 5.7% (Figure 4-4).

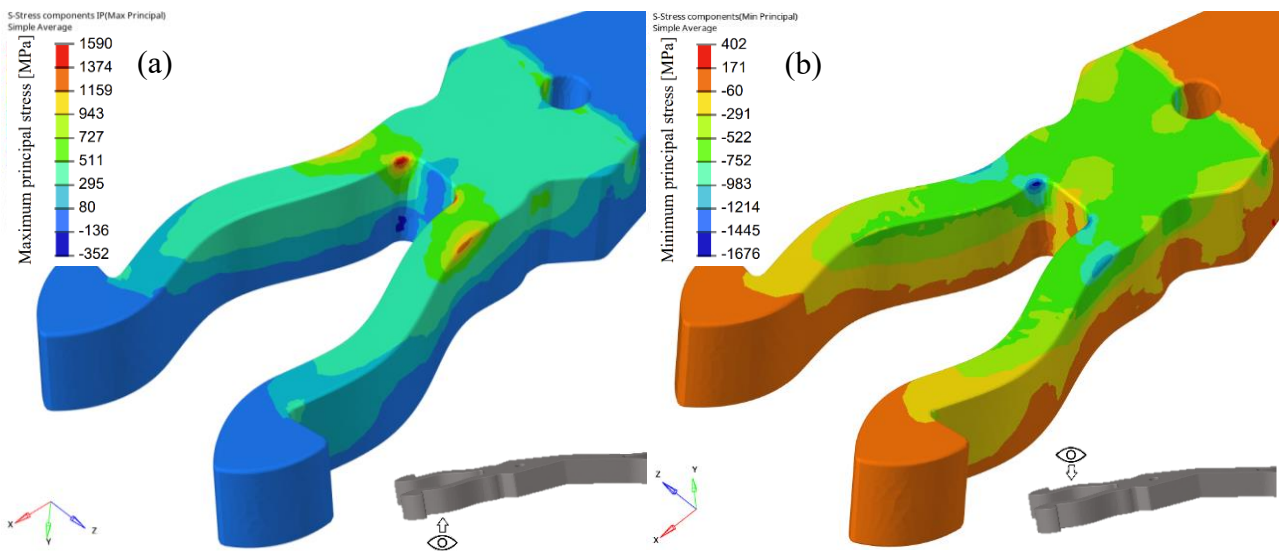


Figure 4-3: (a) Maximum principal stresses of the underside of the Smart Toe II and (b) minimum principal stresses of the upper part after a 7 mm displacement of the distal hooks.

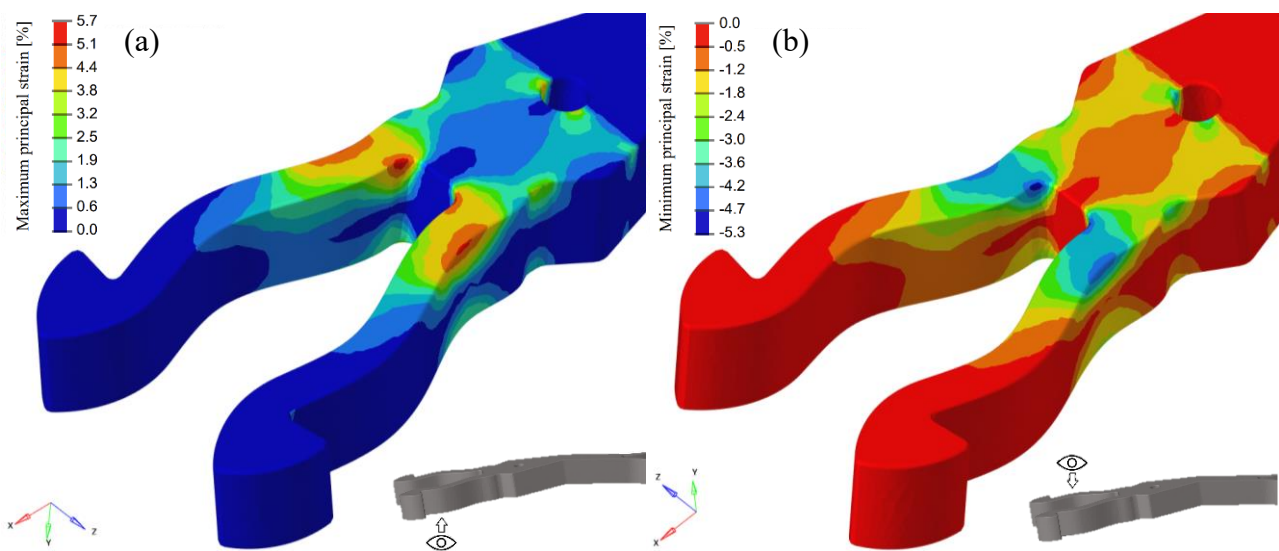


Figure 4-4: (a) Maximum principal strains of the underside of the Smart Toe II and (b) minimum principal strains of the upper part after a 7 mm displacement of the distal hooks.

The bending force required to apply the displacement constraints was then calculated. The graph in Figure 4-5 represents the y displacement of the terminal hook of a single leg as a function of the applied force and as a function of the bending moment generated by a force arm of 6.6 mm. For reference, the 0.7 mm upward displacement of the distal hooks is equivalent to approximately 10° flexion of the device (Figure 4-6). In this extreme situation, the force required to achieve the deformation is 47 N per leg, equivalent to an overall bending moment of 620 Nmm.

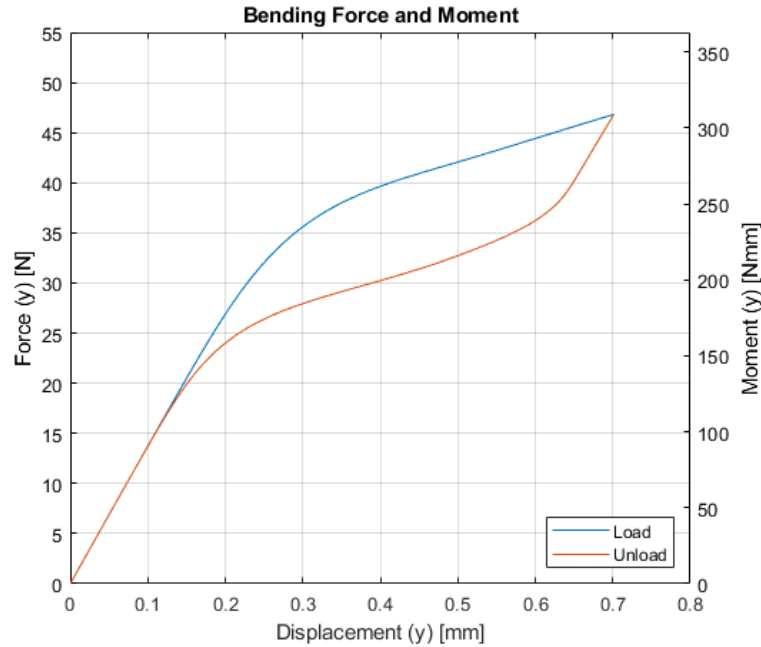


Figure 4-5: Bending force and moment as a function of the y displacement of the distal hooks. The loading phase is plotted in blue (step 1: bending of the device) the unloading phase is plotted in red (step 2: return to the initial position).

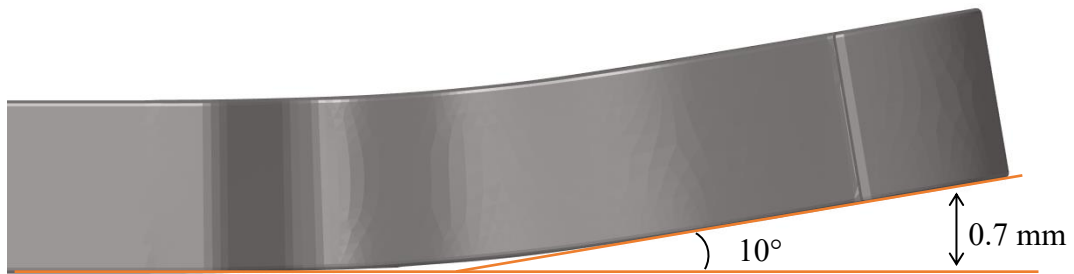


Figure 4-6: 0.7mm upward displacement of the distal hooks is equivalent to approximately 10° flexion of the device

4.3. Fatigue assessment

The equivalent mean strain and strain amplitude were calculated for each element of the FE model using the results obtained from the bending of the implant simulation. The end-of-cycle condition, is the maximum principal stress at the end of the second step of the bending simulation, when the implant returns to the original position. In this situation the strains are null, $\varepsilon_m = 0$. Therefore in the studied case $\varepsilon_m = \varepsilon_a$, and the constant-life diagrams consists of a line with slope 1 (Figure 4-7).

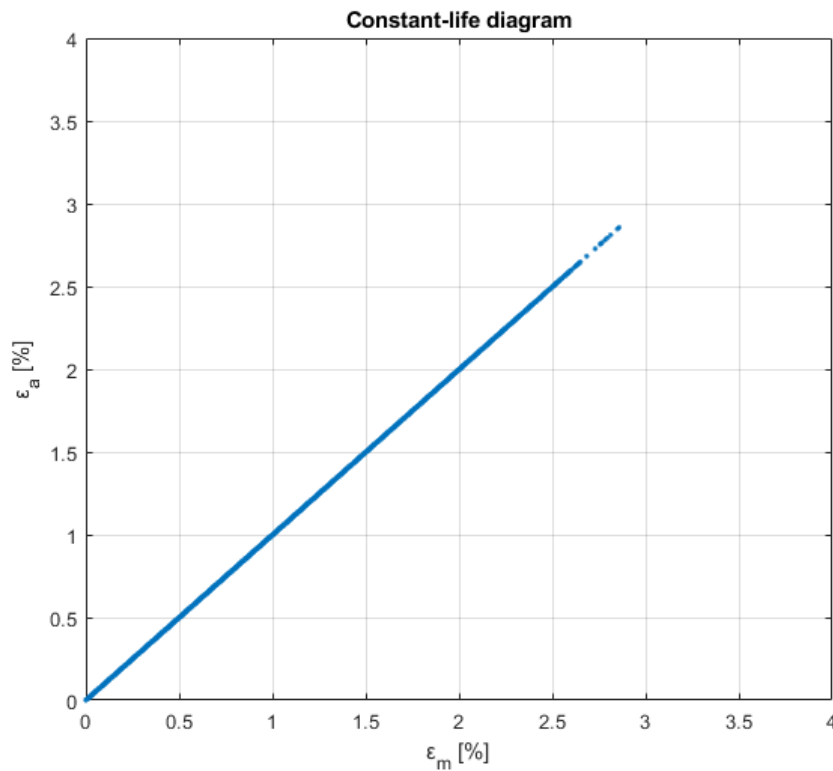


Figure 4-7: Strain-based constant-life diagrams in terms of first principal strains obtained from the results of the bending simulation. ε_a = strain amplitude; ε_m = mean strain.

4.4. Expansion and anchoring of the implant

The analysis has been completed successfully and the computational time was 151 minutes (Intel® Core™ i7-9700K 3.6 Hz processor with 32 GB of RAM). In the first step, the proximal plates moved 0.56 mm towards the device causing its compression. The overall dimensions of the proximal ring in z direction decreased from 3.91 mm to 2.80 mm. The force exerted to reach the predetermined displacement was 25.2 N per plate. Similarly, the distal plates moved 0.93 mm towards the device and the distance between the tips of the distal hooks in z direction decreased from 4.65 mm to 2.80 mm. The force exerted was 26.6 N per plate. In the second step, the plates moved in the opposite direction and the device expanded to its initial position.

Figure 4-8 shows the contact force between implant and plate during compression (load) and expansion (unload) phases as a function of the proximal (ring's z dimension) and distal (distance between the tips of the distal hooks) width of the nail.

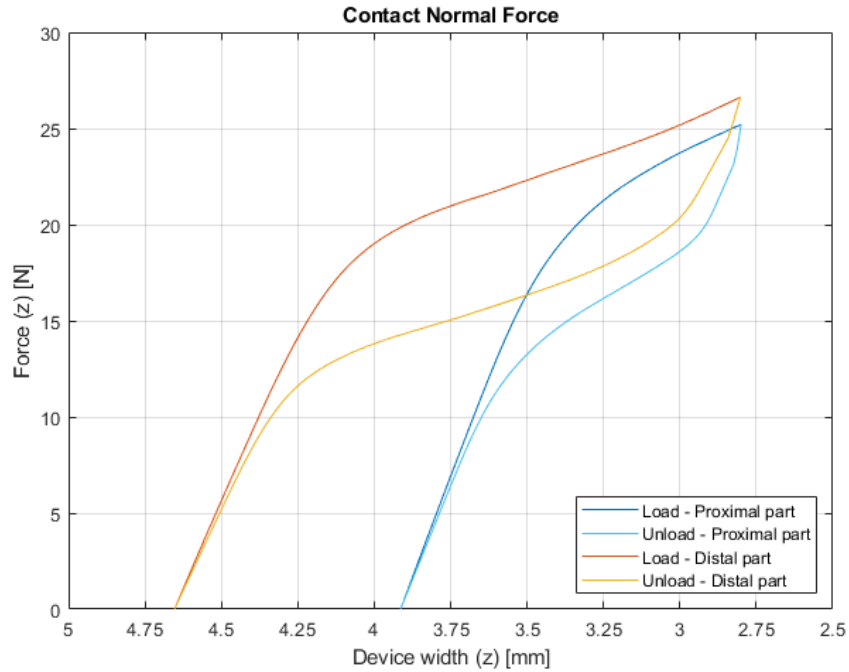


Figure 4-8: Contact normal force as a function of the device width in z. The force trend during the loading (step 1) and unloading (step 2) phase in the proximal part is plotted in blue and light blue respectively. The force trend during the loading (step 1) and unloading (step 2) phase in the distal part is plotted in red and yellow respectively.

The maximum contact force is about 25 N, consequently, multiplying it by the friction coefficient, the anchor force is 17.5 N. The value obtained refers to the force generated by a single contact between nail and bone, to evaluate the overall behavior it must be considered that both in the distal and proximal part there are two surfaces in contact with the bone. The overall contact force in the distal and proximal part is therefore about 35 N. Figure 4-9 shows the trend of the anchor force during the expansion of the nail, analyzing the distal and proximal part separately.

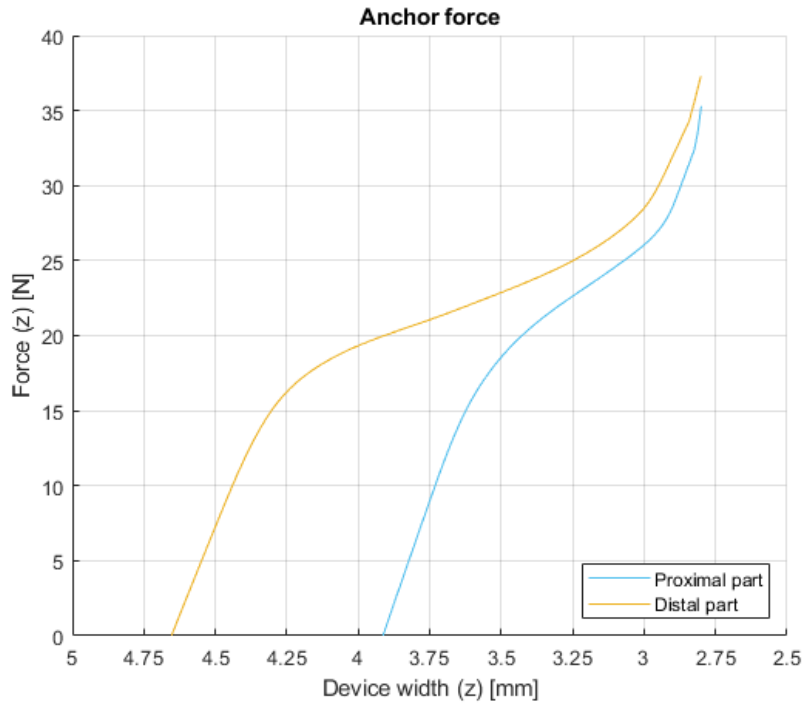


Figure 4-9: Anchor force in the proximal (light blue) and distal (yellow) part as a function of the device width.

After being implanted, during the expansion, the nail reduces its length in x direction by 0.37 mm (from 22.28 to 21.91 mm) and expands its width in the z direction by 1.11 mm in the proximal part and 1.85 mm in the distal part (from 2.80 to 3.91 mm and from 2.80 to 4.65 mm respectively). The increase in the width of the device allows it to adhere to the internal walls of the medullary canal and the implant length reduction results in a compression at the arthrodesis site.

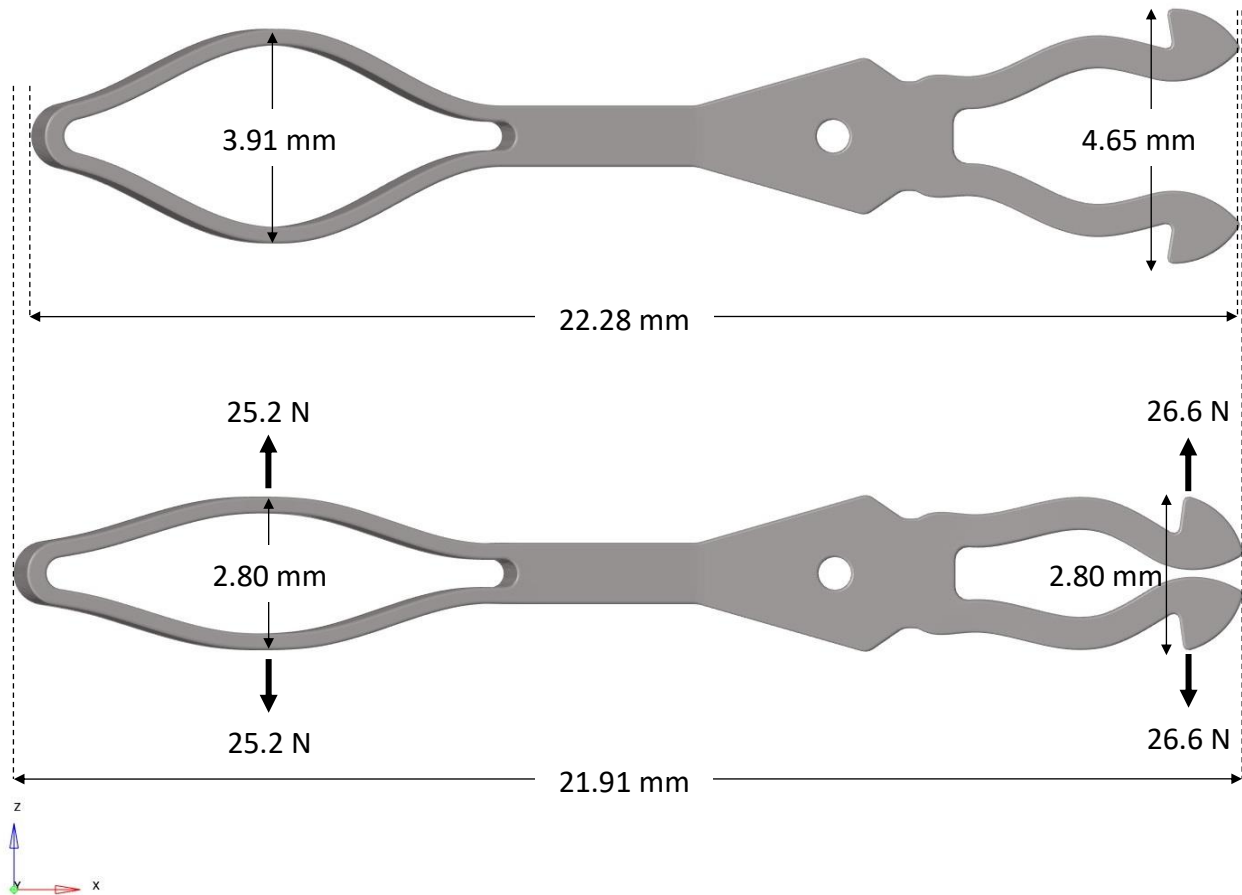


Figure 4-10: Variation of geometric parameters during the change of geometry from expanded (top) to compact shape (down).

To provide a complete mechanical evaluation during nail expansion, stresses and strains were also evaluated in the most stressed conformation, when the nail is compressed. Strain and stress grow as the compression increases. In the proximal part, the most stressed areas are those where the plate and the device make contact and the two parts of the ring with greater curvature (the most proximal and the most distal). The tensile stress reaches a peak of 700 MPa in the inner surface of the ring, in opposite direction to the point of contact with the plates. The maximum compressive stress is in the inner surface of the ring, in the most proximal area, and is 1050 MPa. The maximum compression strain is 3.3% in the contact area between plate and device, while the maximum tensile strain is on the opposite surface and is 4.0% (Figure 4-11).

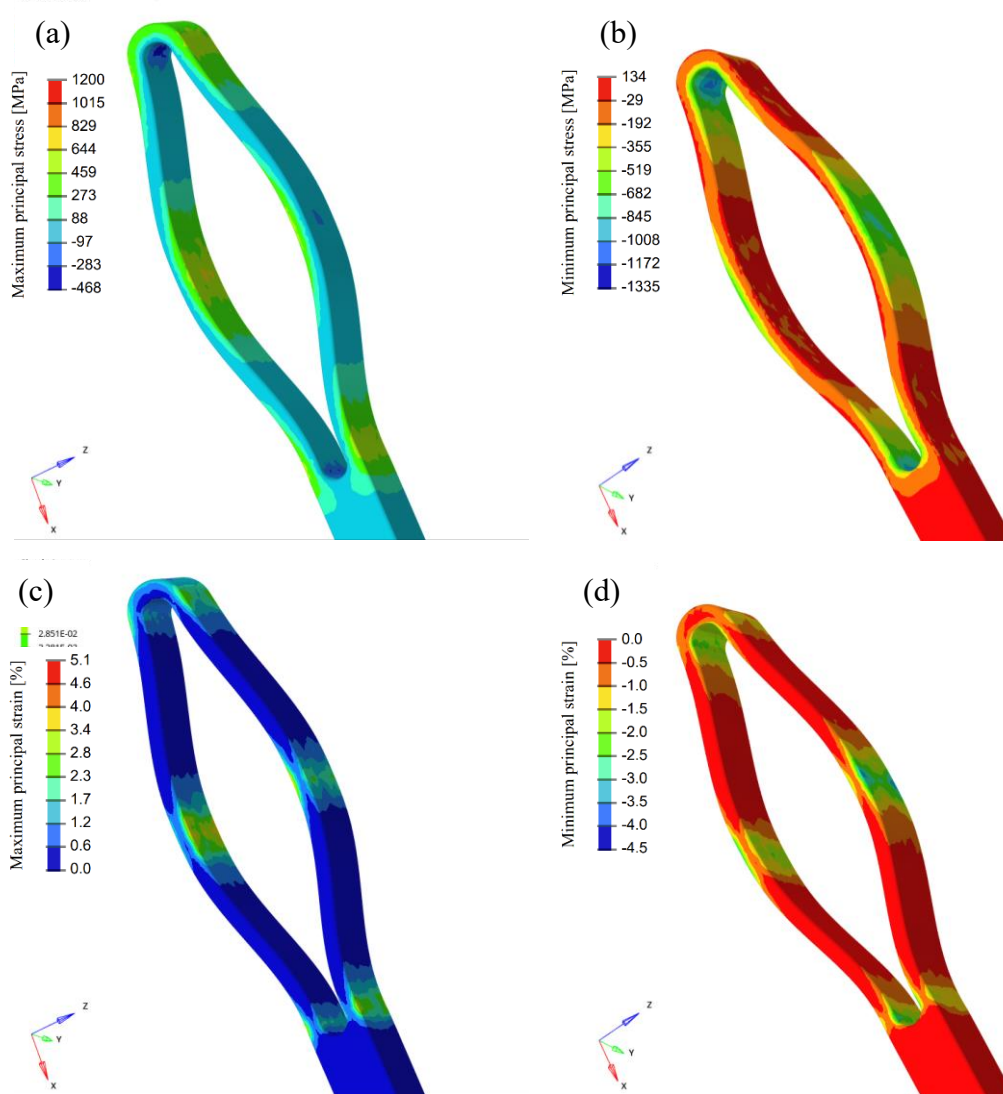


Figure 4-11: (a) Maximum principal stress, (b) minimum principal stress, (c) maximum principal strain, and (d) minimum principal strain in the proximal part of the compressed Smart Toe II model.

In the distal part, the elements most stressed are located at the insertion of the legs in the body of the device. More precisely, the maximum tensile stress is equal to 1200 MPa in the external surface of the leg insertion and the maximum compressive stress is 1335 MPa in the internal surface of the leg insertion. Compressive and tensile strains are located in areas similar to compressive and tensile stresses, with the difference that they are located slightly more distal and close to the fillets. The maximum compressive strain is 4.5%, while the maximum tensile strain is 5.1% (Figure 4-12).

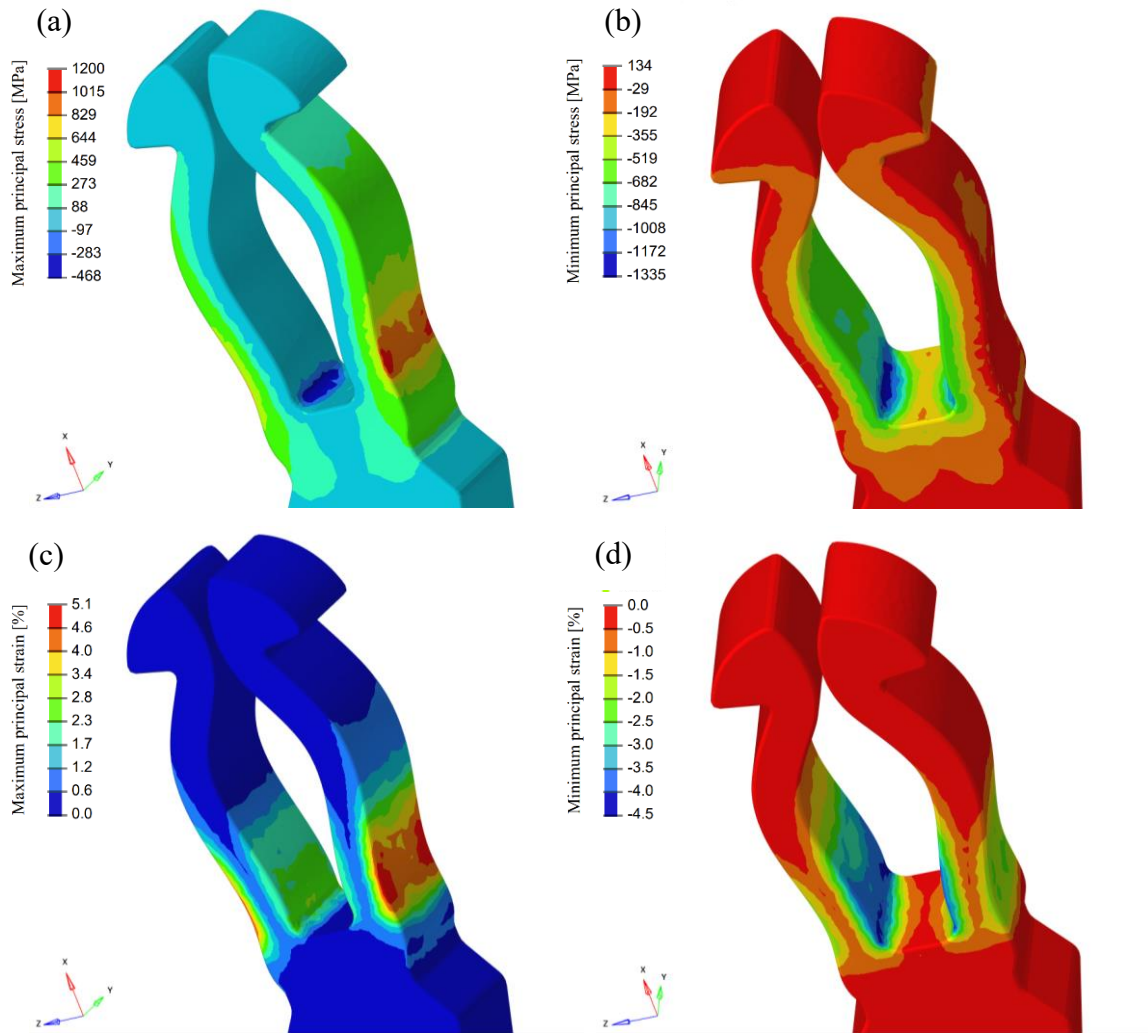


Figure 4-12: (a) Maximum principal stress, (b) minimum principal stress, (c) maximum principal strain, and (d) minimum principal strain in the distal part of the compressed Smart Toe II model.

5. Discussion

Designing a new device or optimizing an existing one is a time-consuming and expensive process. It is necessary to create prototypes, carry out experimental tests, observe the results, change the model accordingly and subsequently repeat these steps. The application of *in silico* simulations is spreading more and more in every field of application because it allows simulating the mechanical behavior of the device during the design process without having to create prototypes or carry out experimental tests.

In this perspective, this work aims to define a numerical framework to evaluate the biomechanical behavior of an IINI. Up to now, no *in silico* study has been proposed to evaluate the mechanical performance of an IINI. Bayod et al. [77] evaluated *in silico* the effects that an IINI has on the phalanges evaluating the reduction of dorsal displacement of the toes phalanges. But an appropriate material model for the Nitinol was not used and the stresses suffered by the device were not evaluated. Their work took into consideration the entire biomechanics of the foot, analyzing bone by bone and modeling cartilage joints and ligaments. The realization of a detailed and complex FE model requires a lot of time both to implement the model and to run the numerical simulations.

The FE simulations conducted in the framework did not take into account the phalanges or the biomechanics of the foot and its joints, but rather used boundary conditions such as displacements assigned to groups of nodes or rigid plates to simplify the model. Thanks to submodeling, the computational time required to run the simulations was relatively short.

5.1. Model verification

The stress-strain curve was evaluated in the most stressed node to be sure to evaluate a complete wider curve. The presence of the hysteresis cycle that characterizes the behavior of Nitinol is evident in both simulations. The parameters interpolated from the curves obtained from the simulations results respect the values set in the model with an acceptable deviation.

The results obtained from the FE simulation are compliant with the simple beam theory for a cantilever beam using the flexure formula. In both cases the most stressed areas are located at the extreme fibers at the top and bottom of the beam, near to the built-in-support, i.e. the insertion of the distal leg. Moreover, when considering the stress intensification factor, the result of the analytical solution is even more similar to that obtained from numerical simulations, explaining why higher stress values occur at the fillets.

5.2. Bending of the implant

Results of FE simulations showed that the most critical point during the flexion of the nail is the insertion of the distal legs. The areas that the simulation results have highlighted as the most stressed in Smart Toe II, coincide with the area where studies reported the most frequent point of rupture of Smart Toe (Figure 5-1). In fact, Obrador et al. [64], Khan et al. [68] and Catena et al. [61] found that the most common Smart Toe fracture site is at the distal thinner legs of the implant. In the study conducted by Scholl et al.[15] the most common fracture site of the Smart Toe implant was at the thinner distal and proximal legs. Payo-Ollero et al. [6] reported two implant ruptures in the proximal legs (19-mm straight, and 20-mm straight SmartmToe implant) and two in the distal legs (16-mm angled Smart Toe implant).

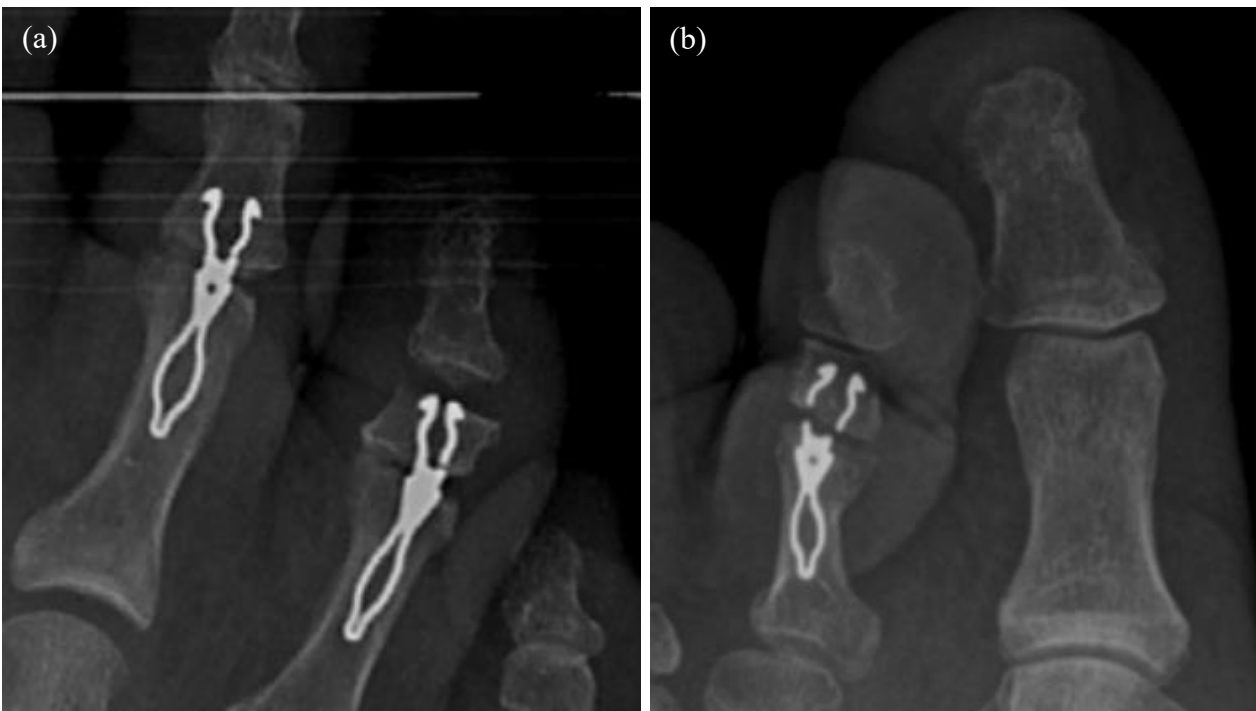


Figure 5-1: Radiographic images representing two cases of rupture of the Smart Toe implant. Picture (a) is adapted from [15]; picture (b) is adapted from [6].

Although the design of the new Smart Toe II has been significantly improved to overcome the criticalities that emerged in clinical practice with the predecessor Smart Toe, the results of the simulations have shown that the most critical area is still the insertion of the distal legs. However, this does not mean that the design improvement was not enough to avert the risk of breakage. The results confirmed the presence of a critical area located at the insertion point of the leg. Numerical and experimental tests should be performed to verify structural integrity in situations of normal use and exceptional situations where the nail could be more stressed. In this work, the simulations conducted aimed to simulate the mechanical stresses to which the device is subjected during walking.

The maximum stresses and strains obtained can be compared with the material strength provided by the material manufacturer to ensure that the values are below a safe threshold.

The nail is expected to flex during use, therefore it is important to be able to predict the strength of the device as the angle of flexion changes. It was possible to establish the maximum load the device can support, and the maximum degree of bending that can be safely achieved without the risk of breaking. Figure 4-5 describes the bending force and moment of a single leg as a function of the device flexion. It was also known the trend of maximum stress and strain as a function of device flexion. Therefore it was possible to derive the device's maximum stress and strain when is applied a certain bending moment or a certain displacement of the distal hooks (Figure 5-2).

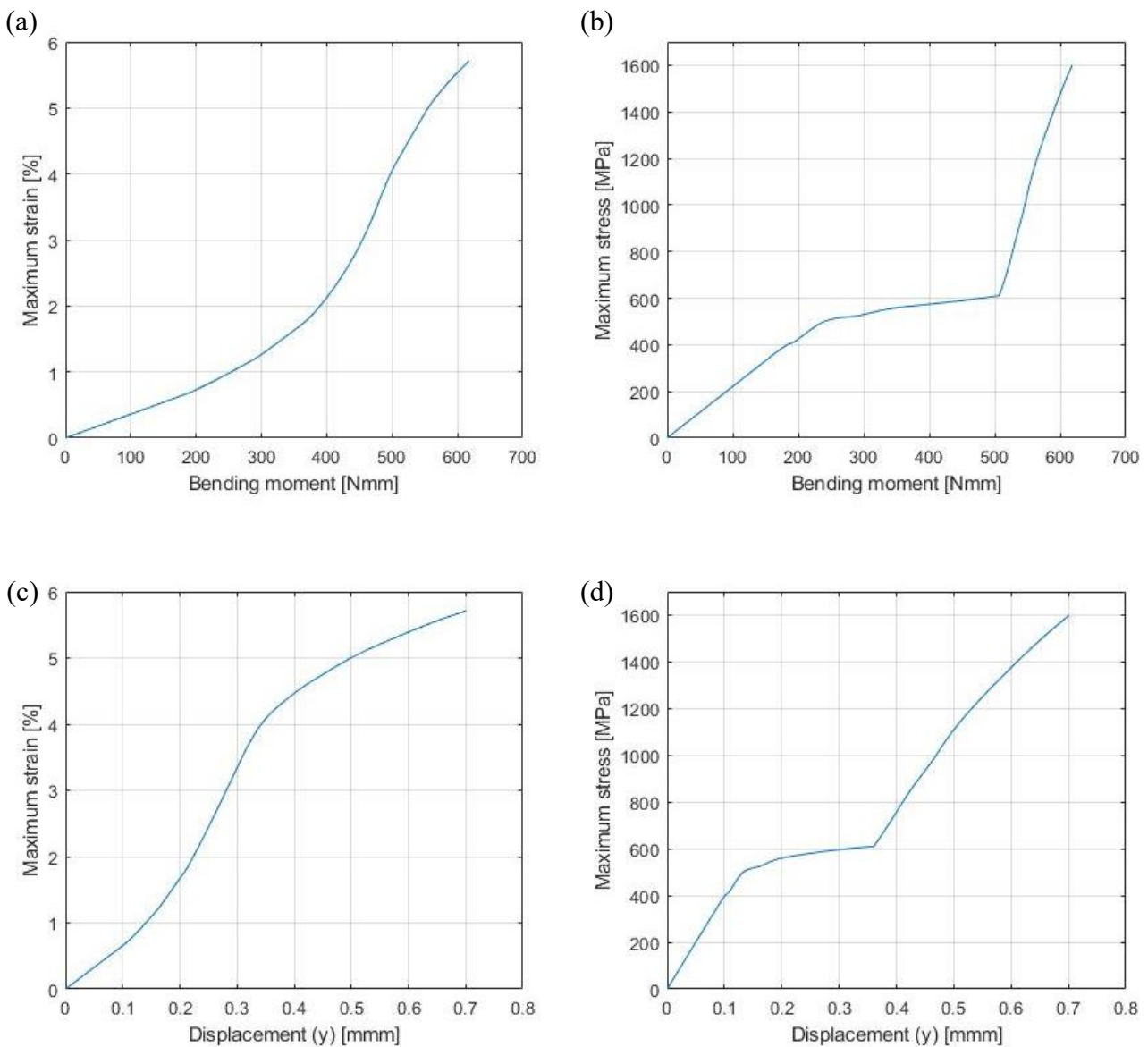


Figure 5-2: Maximum strain (a) and stress (b) curve as a function of the bending moment acting on the distal part of the Smart Toe II model; maximum strain (c) and stress (d) curve as a function of the displacement of the distal hooks.

Since the material supplier provides the rupture stress or strain, it is possible to know already in the design phase what will be the maximum tolerable bending moment and maximum tolerable displacement in z of the distal hooks to which the device can be subjected without breaking.

5.3. Fatigue assessment

The strain-based constant-life uniaxial diagram relative to the bending test of the Smart Toe II is a straight line with unit slope.

The points plotted in Figure 4-7 should be compared with the results obtained from experimental uniaxial tests on a material specimen, to ensure that all points lie under the experimental data curve. When all the points relating to the various nodes of the device fall below the experimental curve, fatigue failure does not occur. In the opposite case, if some points exceed the limit curve, fatigue failure occurs. Experimental tests were not conducted in this work. As an example, has been reported the work by Scalet et al. [84] regarding a Nitinol stent in which the experimental data for the limit curve is taken from the paper by Pelton et al. [43] (Figure 5-3).

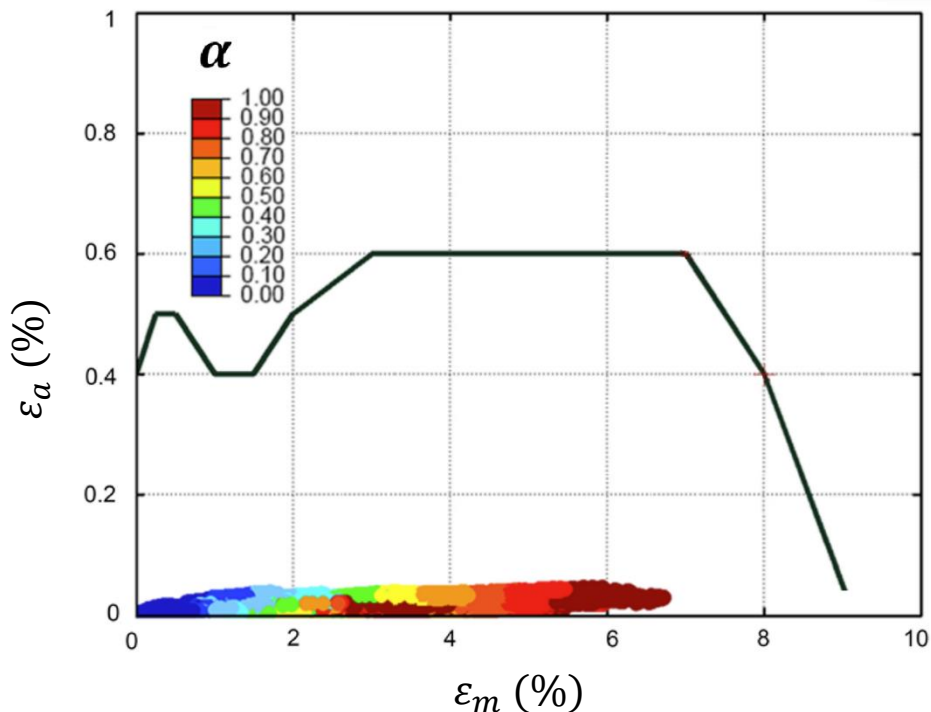


Figure 5-3: Strain-based constant-life diagrams in terms of first principal. The experimental limit curve referred to $N = 10^7$ cycles, is represented as a black line. Each point in the diagrams is colored depending on the corresponding value of the martensite fraction α . Fatigue failure does not occur because all points are under the limit curve. ε_a = strain amplitude; ε_m = mean strain. Graph adapted from [84].

5.4. Expansion and anchoring of the implant

The most evident result of the simulation is the shortening of the device in the x direction and the increase of the width in z . This confirms the correct functional design aimed to provide compression on the arthrodesis site and anchoring to the bone.

The nail, after being implanted, expands its width until it adheres to the bone. The contact between implant and bone generates contact forces and the magnitude is function of how far the nail has to expand to collide with the bone. Simulation results showed that the more the nail expands, the lower the contact force is. Limiting case is when the diameter of the bone canal is equal to or greater than the width of the expanded device, in this case, no contact forces are generated.

The graph in Figure 4-8 shows the presence of a hysteresis cycle, therefore, at the same compression level, the compression force (load) is inferior compared to the contact force (unload) between device and bone. Obviously, in the design phase the contact forces must be maximized and consequently, the hysteresis loop should be reduced. The hysteresis cycle in Figure 4-2 derives from the model of the material used, characterized by the typical behavior of Nitinol in the stress-strain curve. To maximize the contact forces the Nitinol alloy should be chosen in order to increase the start and end stress values for the reverse phase transformations from martensite to austenite.

The curve in Figure 4-8 does not reflect the same trend as the graph shown in Figure 4-2 because it derives from the behavior of all the elements that make up the device, each stressed in a different way. Hence there are elements with major strains, near the insertion point of the distal legs, and elements with minor strains such as those in the body of the device. The force-displacement curve shows the overall behavior of the nail.

The importance of being able to calculate the contact forces and estimate their magnitude derives from the consequent ability to calculate the anchoring forces. They limit the relative movements between bone and implant and therefore allow to predict the risk of implant migration and bone non-union. Anchor forces are also responsible for the compression between the two phalanges, thus promoting arthrodesis. The values shown in Figure 4-9 refer to the condition of complete compression of the device, where the contact forces are maximum. The magnitude of the forces decreases as the nail expands. Depending on the width of the hole drilled in the phalanges the device will expand to a certain size. If a common 3.2 mm drill bit is used, nail expansion will cause an anchor force of approximately 25 N. These values are consistent with the documented compression force of the Super Scaffold IINI device, which generates a mean maximum force of 27.1 N (data obtained experimentally, see Figure 5-4) [88]. Comparing the anchoring force calculated in this work and the compression force in Super scaffold it is observed that in both graphs there is initially a steep

increase in force, then a plateau and finally a steep increase again. This common trend in the two devices mirrors the behavior of Nitinol.

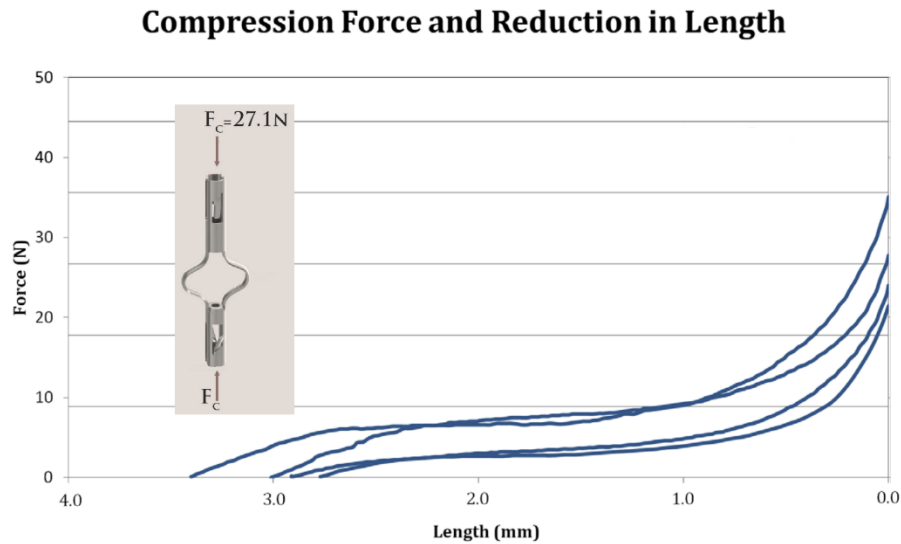


Figure 5-4: Experimental data of the compression force as a function of the Super Scaffold length. Picture adapted from [88].

The graph in Figure 4-9 shows that the behavior in the distal and proximal part is not symmetrical. The difference between the anchor forces is more marked when the device increases its width in z . In this situation, the device does not work efficiently because the device loses its stability with the bone as soon as a force greater than the lesser anchor force of the two is reached, regardless the magnitude of the anchor force on the other side. It does not matter the magnitude of the maximum anchor force, but only the minimum between the distal and the proximal part. This FE simulation allows to verify that the anchor forces are similar in the proximal and distal area. When an imbalance of proximal and distal forces occurs, to make them symmetrical, it is possible to vary the device geometry. In the example in Figure 4-9 the proximal part generates lower anchoring forces, this is mainly due to the lesser width variation in the proximal part. To balance the forces, the device, in the expanded configuration, should have a similar width in the distal and proximal part, or, alternatively the thickness of the ring in the proximal part should be increase to make it stiffer and generate greater contact forces.

5.5. Limits

This work presents a numerical framework to evaluate the biomechanical behavior of an IINI. This is a preliminary study, the real device was not available and no experimental test have been conducted on it, therefore it has limitations.

First, the geometry of the target device was reproduced from drawings, photos and measurements found in datasheets or described in publications. To accurately reproduce the device more sophisticated systems should be used. For example, a three-dimensional acquisition system or a caliper could be used to create three-dimensional geometry which is faithful to the real model.

Second, no mesh convergence analysis was done. This type of analysis allows to evaluate how the simulation outputs change with the variation of the element size in order to establish the optimal one that provides a good compromise between the stability of the result and the computational cost.

Third, it was not possible to carry out an experimental uniaxial test on a Nitinol specimen to obtain the stress-strain curve from which interpolate the material parameters for the material model. Normally this is the standard procedure to make sure that the material implemented in the simulation reflects the real life behavior. Unfortunately, in this case, a Nitinol specimen was not available and therefore data from the literature relating to the most similar device in terms of field of applications and dimensions have been used.

Fourth, the model of the material implemented allows to simulate the superelastic behavior of Nitinol with a good approximation, but does not take into account the plastic deformations. Therefore it was not possible to know whether plastic deformations occur during the FE simulation performed.

Fifth, the model has not been validated. Numerical simulations are a powerful tool for evaluating the mechanical behavior of devices already in the design phase without carrying out expensive and time-consuming experimental tests. But it is essential that the results provided by the *in silico* analyzes are reliable, and to be sure of this, the model must be validated. To validate the model it is necessary to compare the results obtained from the FE simulation with the results of an experimental test with a set up equal to that implemented *in silico*.

6. Conclusion

Technological innovation is reshaping the world faster than ever before. New tools and methods are constantly evolving to develop cutting-edge biomedical devices to better solve clinical problems. In this thesis has been mentioned the interphalangeal joint arthrodesis, a treatment for lesser toe deformities and intractable pain from arthritis. The methods to perform arthrodesis have varied over the years depending on the knowledge and technologies available. Currently, the most adopted solution are K-wires. The performance of this device is excellent but has limits that this concept cannot overcome, including the lack of compression in the arthrodesis site, lack of rotation locking between the phalanges, and all the complications deriving from a body crossing the skin barrier. A new metal alloy, discovered in the 1960s and used for the first time in implantable medical devices in 1989, has recently made it possible to overcome the aforementioned limits. This alloy, called Nitinol, an acronym of the elements that make it up and the name of the laboratory where it was discovered, allows the creation of devices that spontaneously vary the geometry when heated beyond a threshold temperature. Innovative IINIs, have recently been developed to provide compression, lock rotation and be permanent without needing a second surgery for removal. There are four alternatives available on the market but at the moment only Smart Toe has captured the attention of most clinical studies. From the clinical reports has emerged that 5.8 % of the implanted devices broke and 0.5 % migrated. These percentages, although low, are not negligible. Another technology is now available to develop better devices. FE modeling allows to reproduce *in silico* the behavior of an object during its lifetime and designing safer device. Through FE modeling it is possible to apply constraint and load conditions to a faithful reproduction of the device geometry and see how the implant performs from a biomechanical point of view. Since there is no legislation providing standard tests to evaluate IINIs, two simulations were performed based on the two main criticalities found in the literature and previous experimental works.

The first simulation provided stress-strain distribution when the device is subjected to a distal bending, situation that commonly occurs during the push-off phase of the gait. The results allowed to establish the maximum supported bending moment and displacement under normal conditions of use, and to perform preliminary fatigue strength analysis. The most stressed area predicted by the model is the same where studies reported the most frequent point of rupture. The second simulation reproduced the nail expansion in the bone to evaluate the contact forces exchanged. Moreover, known the friction coefficient between the bone and the device, it was possible to calculate the anchor forces, responsible for the compression in the arthrodesis site and the prevention of implant migration.

The FE method is changing the design process of new devices. In this context, the framework created in this work could contribute to the development of better IINIs. In the future, the Smart Toe II implant will be purchased. The device will be scanned to create a more accurate geometric model. Furthermore, experimental tests it will be conduct to the commercial model. Uniaxial tensile test will be performed to derive the parameters for the material model. Also, the simulations developed in this thesis will be reproduced experimentally to validate FE model. The validated model could be used to predict the mechanical strength, effectiveness and safety of IINs and at the same time provided information for its certification. All evaluations will be performed without creating prototypes or conducting experimental tests, hence, times and costs will be significantly reduced compared to a standard design process.

References

- [1] K. Shirzad, C. D. Kiesau, J. K. DeOrio, and S. G. Parekh, “Lesser toe deformities,” *Journal of the American Academy of Orthopaedic Surgeons*, vol. 19, no. 8. Lippincott Williams and Wilkins, pp. 505–514, 2011, doi: 10.5435/00124635-201108000-00006.
- [2] “foot_x_ray_image.” https://prod-images-static.radiopaedia.org/images/8011971/de0f7a7fa8561dc31e023e21a554a3_big_gallery.jpg (accessed Nov. 24, 2021).
- [3] “File:X-ray of normal hand by dorsoplantar projection.jpg - Wikimedia Commons.” https://commons.wikimedia.org/wiki/File:X-ray_of_normal_hand_by_dorsoplantar_projection.jpg (accessed Nov. 24, 2021).
- [4] C. Savvidou and J. Kutz, “Interphalangeal and thumb metacarpophalangeal arthrodesis with an intramedullary implant,” *Ann. Plast. Surg.*, vol. 70, no. 1, pp. 34–37, 2013, doi: 10.1097/SAP.0b013e31821d0757.
- [5] W. H. Seitz and M. E. Marbella, “Distal interphalangeal joint arthrodesis using nitinol intramedullary fixation implants: X-fuse implants for dip arthrodesis,” *Tech. Hand Up. Extrem. Surg.*, vol. 17, no. 3, pp. 169–172, 2013, doi: 10.1097/BTH.0b013e31829ba688.
- [6] J. Payo-Ollero, A. Casajús-Ortega, R. Llombart-Blanco, C. Villas, and M. Alfonso, “The efficacy of an intramedullary nitinol implant in the correction of claw toe or hammertoe deformities,” *Arch. Orthop. Trauma Surg.*, vol. 139, no. 12, pp. 1681–1690, Dec. 2019, doi: 10.1007/s00402-019-03203-w.
- [7] Y. M. Golightly, M. T. Hannan, A. B. Dufour, and J. M. Jordan, “Racial differences in foot disorders and foot type,” *Arthritis Care Res. (Hoboken).*, vol. 64, no. 11, pp. 1756–1759, Nov. 2012, doi: 10.1002/ACR.21752.
- [8] J. C. M. Schrier, J. W. Louwerens, and C. C. P. M. Verheyen, “Opinions on lesser toe deformities among Dutch orthopaedic departments,” *Foot Ankle Int.*, vol. 28, no. 12, pp. 1265–1270, Dec. 2007, doi: 10.3113/FAI.2007.1265.
- [9] J. F. Doty and J. A. Fogleman, “Treatment of Rigid Hammer-Toe Deformity: Permanent Versus Removable Implant Selection,” *Foot and Ankle Clinics*, vol. 23, no. 1. W.B. Saunders, pp. 91–101, Mar. 01, 2018, doi: 10.1016/j.fcl.2017.09.007.
- [10] J. C. M. Schrier, C. C. P. M. Verheyen, and J. W. Louwerens, “Definitions of hammer toe and claw toe,” *J. Am. Podiatr. Med. Assoc.*, vol. 99, no. 3, pp. 194–197, May 2009, doi: 10.7547/0980194.
- [11] Coughlin M and Mann R, *Surgery of the Foot and Ankle*, vol. 1. Mosby, Philadelphia, 1999.

- [12] M. S. Myerson and M. J. Shereff, "The pathological anatomy of claw and hammer toes," *J. Bone Jt. Surg. - Ser. A*, vol. 71, no. 1, pp. 45–49, 1989, doi: 10.2106/00004623-198971010-00008.
- [13] W. Trethowan, "The treatment of hammer-toe, Part 1—general considerations: conservative measures prophylaxis," *Lancet*, vol. 1, pp. 1257–1258, 1925.
- [14] J. S. Sandhu, W. T. DeCarbo, and M. H. Hofbauer, "Digital Arthrodesis With a One-Piece Memory Nitinol Intramedullary Fixation Device: A Retrospective Review," *Foot Ankle Spec.*, vol. 6, no. 5, pp. 364–366, Oct. 2013, doi: 10.1177/1938640013496458.
- [15] A. Scholl, J. McCarty, D. Scholl, and A. Mar, "Smart toe® implant versus buried kirschner wire for proximal interphalangeal joint arthrodesis: A comparative study," *J. Foot Ankle Surg.*, vol. 52, no. 5, pp. 580–583, Sep. 2013, doi: 10.1053/j.jfas.2013.02.007.
- [16] M. J. Coughlin, J. Dorris, and E. Polk, "Operative repair of the fixed hammertoe deformity," *Foot Ankle Int.*, vol. 21, no. 2, pp. 94–104, Feb. 2000, doi: 10.1177/107110070002100202.
- [17] J. J. Stapelton, *Foot and ankle arthrodesis*, 1st ed., vol. 34–3. Elsevier, 2017.
- [18] W. C. Kramer, M. Parman, and R. M. Marks, "Hammertoe correction with k-wire fixation," *Foot Ankle Int.*, vol. 36, no. 5, pp. 494–502, May 2015, doi: 10.1177/1071100714568013.
- [19] C. Zingas, D. A. Katcherian, and K. K. Wu, "Kirschner Wire Breakage after Surgery of the Lesser Toes," *Foot Ankle Int.*, vol. 16, no. 8, pp. 504–509, Jun. 1995, doi: 10.1177/107110079501600809.
- [20] C. O’Kane and T. Kilmartin, "Review of Proximal Interphalangeal Joint Excisional Arthroplasty for the Correction of Second Hammer Toe Deformity in 100 Cases:," <http://dx.doi.org/10.1177/107110070502600408>, vol. 26, no. 4, pp. 320–325, Jun. 2016, doi: 10.1177/107110070502600408.
- [21] S. F. Taylor RG, "An Operative Procedure for the Treatment of Hammer-Toe and Claw-Toe," *J Bone Jt. Surg*, vol. 22, no. Issue 3, p. 608, 1940.
- [22] W. H. B. Edwards and A. D. Beischer, "Interphalangeal joint arthrodesis of the lesser toes," *Foot Ankle Clin.*, vol. 7, no. 1, pp. 43–48, Mar. 2002, doi: 10.1016/S1083-7515(02)00002-5.
- [23] R. Caterini, P. Farsetti, U. Tarantino, V. Potenza, and E. Ippolito, "Arthrodesis of the Toe Joints with an Intramedullary Cannulated Screw for Correction of Hammertoe Deformity:," <http://dx.doi.org/10.1177/107110070402500411>, vol. 25, no. 4, pp. 256–261, Jun. 2016, doi: 10.1177/107110070402500411.
- [24] G. Imhäuser, "[Operation of hammer toes and claw toes, and treatment of unfavourable results (author’s transl)].," *Z. Orthop. Ihre Grenzgeb.*, vol. 117, no. 2, pp. 179–84, Apr. 1979, [Online]. Available: <http://www.ncbi.nlm.nih.gov/pubmed/380202>.

- [25] M. Guelfi, A. Pantalone, J. C. Daniel, D. Vanni, M. G. B. Guelfi, and V. Salini, “Arthrodesis of proximal inter-phalangeal joint for hammertoe: intramedullary device options,” *Journal of Orthopaedics and Traumatology*, vol. 16, no. 4. Springer-Verlag Italia s.r.l., pp. 269–273, Jun. 27, 2015, doi: 10.1007/s10195-015-0360-0.
- [26] Stryker, “X Fuse Superelastic Implant, Operative Technique.” Accessed: Jun. 20, 2021. [Online]. Available: <https://www.strykermeded.com/media/1605/x-fuse-superelastic-implant.pdf>.
- [27] Stryker, “Intramedullary Implant Smart Toe II, Operative Technique,” 2015. Accessed: May 30, 2021. [Online]. Available: <https://www.stryker.com/us/en/foot-and-ankle/products/smart-toe-ii.html>.
- [28] Metric, “Super Scaffold, intramedullary Fixation System.” Accessed: Jun. 20, 2021. [Online]. Available: <http://metricmd.com/wp-content/uploads/2016/02/Brochures.pdf>.
- [29] “Instructions for Use HAMMERLOCK™ 2 Intramedullary Nitinol Implant System,” 2020. Accessed: May 30, 2021. [Online]. Available: https://ifu.depuysynthes.com/binary/org/DPY_SYN_EMEA/ifu_documents/Trauma/SE_801368_AA_eng_LR.pdf.
- [30] W. J. Buehler, *Personal communication*. .
- [31] J. CHRISTIAN, “Constitution of binary alloys (Second edition), by M. Hansen, with the cooperation of K. Anderko. Pp. xix + 1305. McGraw-Hill Book Co. Inc., New York; McGraw-Hill Publishing Co. Ltd, London. 1958. E12 12s. net,” *Endeavour*, vol. 18, no. 71, p. 165, 1959, doi: 10.1016/0160-9327(59)90213-3.
- [32] W. J. Buehler, *Letter to Amy Axt Hanson*. .
- [33] G. B. KAUFFMAN and I. MAYO, “The Story of Nitinol: The Serendipitous Discovery of the Memory Metal and Its Applications,” *Chem. Educ.*, vol. 2, no. 2, pp. 1–21, 1997, doi: 10.1007/s00897970111a.
- [34] D. Kapoor, “Nitinol for Medical Applications: A Brief Introduction to the Properties and Processing of Nickel Titanium Shape Memory Alloys and their Use in Stents,” *Johnson Matthey Technology Review*, vol. 61, no. 1. pp. 66–76, 2017, doi: 10.1595/205651317X694524.
- [35] L. M. Schetky, “Shape-memory alloys.,” *SCI. AM.*, vol. 241, no. 5, Nov. 1979, pp. 68–76, 1979, doi: 10.1038/scientificamerican1179-74.
- [36] “GII® Anchor | Mitek Suture Anchor | J&J Medical Devices.” <https://www.jnjmedicaldevices.com/en-US/product/giir-anchor> (accessed Nov. 27, 2021).
- [37] “Filtro cavale - SIMON NITINOL® - Bard Medical.” <https://www.medicalexpo.it/prod/bard->

medical/product-78646-918065.html (accessed Nov. 27, 2021).

- [38] *ASTM F2005 - 21 Standard Terminology for Nickel-Titanium Shape Memory Alloys*, vol. 13.01. 2021.
- [39] A. Biscarini, G. Mazzolai, and A. Tuissi, “Enhanced Nitinol Properties for Biomedical Applications,” *Recent Pat. Biomed. Eng.*, vol. 1, pp. 180–196, 2008, doi: 10.2174/1874764710801030180.
- [40] V. Valentina, “Materiali a Memoria di Forma: caratterizzazione e applicazioni nel campo dei Beni Culturali,” Università di Bologna, 2008.
- [41] D. J. Hoh, B. L. Hoh, A. P. Amar, and M. Y. Wang, “Shape memory alloys: Metallurgy, biocompatibility, and biomechanics for neurosurgical applications,” *Neurosurgery*, vol. 64, no. SUPPL. 5, 2009, doi: 10.1227/01.NEU.0000330392.09889.99.
- [42] Center for Devices and Radiological Health, “Technical Considerations for Non-Clinical Assessment of Medical Devices containing Nitinol,” Jul. 2015. Accessed: Jul. 28, 2021. [Online]. Available: <https://www.fda.gov/regulatory-information/search-fda-guidance-documents/technical-considerations-non-clinical-assessment-medical-devices-containing-nitinol>.
- [43] A. R. Pelton, “Nitinol fatigue: A review of microstructures and mechanisms,” in *Journal of Materials Engineering and Performance*, Jul. 2011, vol. 20, no. 4–5, pp. 613–617, doi: 10.1007/s11665-011-9864-9.
- [44] P. J. Doherty, R. L. Williams, D. F. Williams, and A. J. C. Lee, “Biomaterial-Tissue Interfaces: proceedings of the Ninth European Conference on Biomaterials, Chester, U.K., September 9-11, 1991,” *Advances in Biomaterials*, vol. 10. European Society for Biomaterials, Chester, U.K., p. 533, Sep. 1992, Accessed: May 27, 2021. [Online]. Available: https://onsearch.library.rice.edu/discovery/fulldisplay/alma991023008279705251/01RICE_INST:RICE.
- [45] D. F. Williams, *The Williams Dictionary of Biomaterials*. Liverpool University Press, 1999.
- [46] D. Williams, “Revisiting the definition of biocompatibility.,” *Med. Device Technol.*, vol. 14, no. 8, pp. 10–3, Oct. 2003, Accessed: May 27, 2021. [Online]. Available: <http://www.ncbi.nlm.nih.gov/pubmed/14603712>.
- [47] B. D. Ratner, A. S. Hoffman, F. J. Schoen, and J. E. Lemons, “Introduction - Biomaterials Science: An Evolving, Multidisciplinary Endeavor,” *Biomaterials Science: An Introduction to Materials: Third Edition*. Elsevier Inc., pp. xxv–xxxix, Jan. 01, 2013, doi: 10.1016/B978-0-08-087780-8.00153-4.
- [48] J. Ryhänen, “Biocompatibility of Nitinol,” *Minimally Invasive Therapy and Allied*

- Technologies*, vol. 9, no. 2. Health Media Ltd./Isis Medical Media Ltd., pp. 99–105, 2000, doi: 10.3109/13645700009063056.
- [49] M. Anke, B. Groppe, H. Kronemann, and M. Grün, “Nickel--an essential element,” *IARC scientific publications*, no. 53. pp. 339–365, Jan. 01, 1984, Accessed: May 27, 2021. [Online]. Available: <https://europepmc.org/article/med/6398286>.
- [50] J. Putters, D. M. K. S. Kaulesar Suku, G. R. Dezeeuw, A. Bijma, and P. A. Besselink, “Comparative cell culture effects of shape memory metal (Nitinol®), nickel and titanium: A biocompatibility estimation,” *Eur. Surg. Res.*, vol. 24, no. 6, pp. 379–382, 1992, doi: 10.1159/000129231.
- [51] P. G. Laing, A. B. Ferguson, and E. S. Hodge, “Tissue reaction in rabbit muscle exposed to metallic implants,” *J. Biomed. Mater. Res.*, vol. 1, no. 1, pp. 135–149, 1967, doi: 10.1002/jbm.820010113.
- [52] J. Black and G. Hastings, *Handbook of Biomaterial Properties*. Springer US, 1998.
- [53] D. J. Wever, A. G. Veldhuizen, M. M. Sanders, J. M. Schakenraad, and J. R. Van Horn, “Cytotoxic, allergic and genotoxic activity of a nickel-titanium alloy,” *Biomaterials*, vol. 18, no. 16, pp. 1115–1120, Aug. 1997, doi: 10.1016/S0142-9612(97)00041-0.
- [54] Biological and clinical evaluation of medical devices, *ISO 10993, Biological evaluation of medical devices*, 5th ed. 2018.
- [55] S. A. Shabalovskaya, “On the nature of the biocompatibility and on medical applications of NiTi shape memory and superelastic alloys,” *Biomed. Mater. Eng.*, vol. 6, no. 4, pp. 267–289, Jan. 1996, doi: 10.3233/bme-1996-6405.
- [56] M. Es-Souni, M. Es-Souni, and H. Fischer-Brandies, “Assessing the biocompatibility of NiTi shape memory alloys used for medical applications,” *Analytical and Bioanalytical Chemistry*, vol. 381, no. 3. Springer, pp. 557–567, Feb. 20, 2005, doi: 10.1007/s00216-004-2888-3.
- [57] G. Rondelli and B. Vicentini, “Localized corrosion behaviour in simulated human body fluids of commercial Ni-Ti orthodontic wires,” *Biomaterials*, vol. 20, no. 8, pp. 785–792, Apr. 1999, doi: 10.1016/S0142-9612(98)90233-2.
- [58] F. Auricchio, R. L. Taylor, and J. Lubliner, “Shape-memory alloys: Macromodelling and numerical simulations of the superelastic behavior,” *Comput. Methods Appl. Mech. Eng.*, vol. 146, no. 3–4, pp. 281–312, Jul. 1997, doi: 10.1016/S0045-7825(96)01232-7.
- [59] F. Auricchio and R. L. Taylor, “Shape-memory alloys: Modelling and numerical simulations of the finite-strain superelastic behavior,” *Comput. Methods Appl. Mech. Eng.*, vol. 143, no. 1–2, pp. 175–194, Apr. 1997, doi: 10.1016/S0045-7825(96)01147-4.
- [60] “Superelasticity - Abaqus documentations.” <https://abaqus->

- docs.mit.edu/2017/English/SIMACAEMATRefMap/simamat-c-superelasticity.htm (accessed Jul. 26, 2021).
- [61] F. Catena, J. F. Doty, J. Jastifer, M. J. Coughlin, and F. Stevens, “Prospective study of hammertoe correction with an intramedullary implant,” *Foot Ankle Int.*, vol. 35, no. 4, pp. 319–325, Jan. 2014, doi: 10.1177/1071100713519780.
- [62] “HAMMERLOCK® 2 | Nitinol Implant | J&J Medical Devices.” <https://www.jnjmedicaldevices.com/en-US/product/hammerlockr-2-nitinol-implant> (accessed May 30, 2021).
- [63] A. K. Angirasa, M. J. Barrett, and D. Silvester, “SmartToe® Implant Compared with Kirschner Wire Fixation for Hammer Digit Corrective Surgery: A Review of 28 Patients,” *J. Foot Ankle Surg.*, vol. 51, no. 6, pp. 711–713, Nov. 2012, doi: 10.1053/j.jfas.2012.06.013.
- [64] C. Obrador, M. Losa-Iglesias, R. Becerro-de-Bengoa-Vallejo, and C. A. Kabbash, “Comparative Study of Intramedullary Hammertoe Fixation,” *Foot Ankle Int.*, vol. 39, no. 4, pp. 415–425, Apr. 2018, doi: 10.1177/1071100717745854.
- [65] M. Ferrier, J. C. Mattei, R. Desmarchelier, M. Fessy, and J. L. Besse, “Radiographic and Clinical Comparison of Proximal Interphalangeal Joint Arthrodesis Between a Static and Dynamic Implant,” *J. Foot Ankle Surg.*, vol. 58, no. 4, pp. 657–662, 2019, doi: 10.1053/j.jfas.2018.11.004.
- [66] D. J. Cuttica, W. DeCarbo, W. B. Smith, and G. C. Berlet, “New intramedullary implant for proximal interphalangeal joint arthrodesis,” *Tech. Foot Ankle Surg.*, vol. 7, no. 3, pp. 203–206, Sep. 2008, doi: 10.1097/BTF.0B013E3181839FBC.
- [67] M. Delmi, “Hammer Toe Surgical Correction, Arthrodesis of the Proximal Interphalangeal (PIP) Joint Using a New Shape Memory Intramedullary Implant,” [Online]. Available: <https://www.yumpu.com/en/document/read/9110842/hammer-toe-surgical-correction-mmi-usacom>.
- [68] F. Khan, S. Kimura, T. Ahmad, D. D’Souza, and L. D’Souza, “Use of Smart Toe© implant for small toe arthrodesis: A smart concept?,” *Foot Ankle Surg.*, vol. 21, no. 2, pp. 108–112, Jun. 2015, doi: 10.1016/j.fas.2014.10.003.
- [69] T. S. Roukis, “A 1-Piece Shape-Metal Nitinol Intramedullary Internal Fixation Device for Arthrodesis of the Proximal Interphalangeal Joint in Neuropathic Patients With Diabetes,” *Foot Ankle Spec.*, vol. 2, no. 3, pp. 130–134, May 2009, doi: 10.1177/1938640009336199.
- [70] M. Jakubek, M. Enzendorfer, R. Fiala, and K. Trieb, “Interphalangeal arthrodesis using an intramedullary nitinol implant: A prospective study,” *Eklem Hast. ve Cerrahisi*, vol. 28, no. 2, pp. 87–91, 2017, doi: 10.5606/ehc.2017.52924.

- [71] Y. K. De Almeida, L. Athlani, F. Dap, and G. Dautel, “Distal interphalangeal joint arthrodesis using the X-Fuse® implant: A retrospective study of 54 fingers with 24 months’ follow-up,” *Hand Surg. Rehabil.*, vol. 38, no. 3, pp. 186–190, 2019, doi: 10.1016/j.hansur.2019.01.001.
- [72] T. Ameline, V. Bégot, L. Ardouin, C. Hulet, and N. Hanouz, “Arthrodesis of thumb interphalangeal and finger distal interphalangeal joints using the intramedullary X-Fuse® implant: Retrospective analysis of 38 cases,” *Chir. Main*, vol. 34, no. 2, pp. 67–72, 2015, doi: 10.1016/j.main.2015.01.002.
- [73] W. S. Pietrzak, T. P. Lessek, and S. V. Perns, “A Bioabsorbable Fixation Implant for Use in Proximal Interphalangeal Joint (Hammer Toe) Arthrodesis: Biomechanical Testing in a Synthetic Bone Substrate,” *J. Foot Ankle Surg.*, vol. 45, no. 5, pp. 288–294, Sep. 2006, doi: 10.1053/j.jfas.2006.05.004.
- [74] J.-Y. Coillard, G. J. Petri, G. van Damme, P. Deprez, and O. Laffenêtre, “Stabilization of Proximal Interphalangeal Joint in Lesser Toe Deformities With an Angulated Intramedullary Implant,” <http://dx.doi.org/10.1177/1071100713519601>, vol. 35, no. 4, pp. 401–407, Jan. 2014, doi: 10.1177/1071100713519601.
- [75] ASTM, “f1264-16 Standard Specification and Test Methods for Intramedullary Fixation Devices.” Accessed: Nov. 22, 2021. [Online]. Available: <https://www.astm.org/f1264-16e01.html>.
- [76] S. D. Rothermel, U. Aydogan, E. P. Roush, and G. S. Lewis, “Proximal Interphalangeal Arthrodesis of Lesser Toes Utilizing K-Wires Versus Expanding Implants: Comparative Biomechanical Cadaveric Study,” *Foot Ankle Int.*, vol. 40, no. 2, pp. 231–236, 2019, doi: 10.1177/1071100718805066.
- [77] J. B. López, R. B. De Bengoa Vallejo, M. E. L. Iglesias, K. T. Jules, and M. Doblaré, “Reduction of dorsal displacement of the proximal and middle phalanges using a neutral or angled implant for joint arthrodesis to treat hammertoe deformity a finite element study,” *J. Am. Podiatr. Med. Assoc.*, vol. 105, no. 6, pp. 493–502, Nov. 2015, doi: 10.7547/14-032.1.
- [78] “Submodeling analysis- Abaqus documentations.” <https://abaqus-docs.mit.edu/2017/English/SIMACAETHERefMap/simathe-c-submodeling.htm>.
- [79] O. Subasi *et al.*, “Theoretical and experimental studies for an orthopedic staple made up Nitinol,” *J. Mech. Behav. Biomed. Mater.*, vol. 62, no. 11, pp. 83–92, 2015, doi: 10.1007/s11665-011-9883-6.
- [80] O. Subasi, S. Torabnia, and I. Lazoglu, “In silico analysis of Superelastic Nitinol staples for trans-sternal closure,” *J. Mech. Behav. Biomed. Mater.*, vol. 107, no. March, p. 103770, 2020, doi: 10.1016/j.jmbbm.2020.103770.

- [81] A. F. Saleeb, B. Dhakal, and J. S. Owusu-Danquah, “Assessing the performance characteristics and clinical forces in simulated shape memory bone staple surgical procedure: The significance of SMA material model,” *Comput. Biol. Med.*, vol. 62, pp. 185–195, 2015, doi: 10.1016/j.combiomed.2015.04.010.
- [82] M. Ackermann, L. Čapek, M. Ackermann, and L. Čapek, “Numerical durability evaluation of Nitinol stent,” *Comput. Methods Biomech. Biomed. Engin.*, vol. 15, no. S1, pp. 99–101, 2012, doi: 10.1080/10255842.2012.713625.
- [83] D. Allegretti, F. Berti, F. Migliavacca, G. Pennati, and L. Petrini, “Fatigue Assessment of Nickel–Titanium Peripheral Stents: Comparison of Multi-Axial Fatigue Models,” *undefined*, vol. 4, no. 1, pp. 186–196, Mar. 2018, doi: 10.1007/S40830-018-0150-7.
- [84] G. Scalet, C. Menna, A. Constantinescu, and F. Auricchio, “A computational approach based on a multiaxial fatigue criterion combining phase transformation and shakedown response for the fatigue life assessment of Nitinol stents:,” <https://doi.org/10.1177/1045389X18798957>, vol. 29, no. 19, pp. 3710–3724, Sep. 2018, doi: 10.1177/1045389X18798957.
- [85] F. Auricchio, A. Constantinescu, C. Menna, and G. Scalet, “A shakedown analysis of high cycle fatigue of shape memory alloys,” *Int. J. Fatigue*, vol. 87, pp. 112–123, 2016, doi: 10.1016/j.ijfatigue.2016.01.017.
- [86] R. J. M. M. Pijpers, H. M. Slot, R. J. M. M. Pijpers, and H. M. Slot, “Friction coefficients for steel to steel contact surfaces in air and seawater,” in *Journal of Physics: Conference Series*, Oct. 2020, vol. 1669, no. 1, p. 012002, doi: 10.1088/1742-6596/1669/1/012002.
- [87] Y. Xu, Y. Yin, and T. Xia, “Study on Fretting Friction Coefficient between NiTi Shape Memory Alloy and Human Bone in Hank’s Solution,” *Rare Met. Mater. Eng.*, vol. 37, no. 7, pp. 1201–1205, Jul. 2008, doi: 10.1016/S1875-5372(09)60032-1.
- [88] Metric, “Technical Documents - Intramedullary Fixation Scaffold (IFS™) System.” [Online]. Available: <http://metricmd.com/wp-content/uploads/2016/02/Metric-Technology-Sheets20160208.pdf>.